Title
High-Throughput Single-Molecule Diffusivity Analysis: New Approaches and Applications

Permalink
https://escholarship.org/uc/item/7dw2k864

Author
Park, Ha Hyung

Publication Date
2023

Peer reviewed|Thesis/dissertation

High-Throughput Single-Molecule Diffusivity Analysis:
New Approaches and Applications

By

Ha Hyung Park

A dissertation submitted in partial satisfaction of the

requirements for the degree of

Doctor of Philosophy

in

Chemistry

in the

Graduate Division

of the

University of California, Berkeley

Committee in charge:

Professor Ke Xu, Chair
Professor Stephen R. Leone
Professor David G. Drubin

Spring 2023

High-Throughput Single-Molecule Diffusivity Analysis:
New Approaches and Applications

Abstract

High-Throughput Single-Molecule Diffusivity Analysis: New Approaches and Applications

by

Ha Hyung Park

Doctor of Philosophy in Chemistry

University of California, Berkeley

Professor Ke Xu, Chair

Following the popularization of super-resolution microscopy for biological research, the advent of functional super-resolution microscopy enabled decoding high-throughput single-molecule signals in single-molecule localization microscopy (SMLM) and extracting multiple physical parameters beyond the structure of the target system. Among those parameters, the diffusivity of single molecules has provided deeper insight into biological systems as diffusion is one of the key mechanisms that carry out life processes and as the diffusivity reflects multiple physicochemical parameters and thus properties of the microenvironment. This dissertation describes applications of the recently developed wide-field ultrahigh-throughput diffusion coefficient analysis and a new method that enables the equivalent measurement without sophisticated hardware setup. By extensively tracking diffusion behaviors of proteins in nanometer-sized matrix structured hydrogel, I drew a comprehensive picture of how different sizes of meshwork affect the protein diffusion coefficients, as well as how such an effect is differentiated by the relative size of proteins to the meshwork. Then, I introduce a new approach to extract diffusion coefficients out of conventional SMLM by incorporating single-molecule image processing through a convolutional neural network. In the last chapter, I summarized efforts on taking the SMLM diffusion analysis to a greater extent.

Table of Contents

List of Figures

Acknowledgements

I am profoundly grateful for the unwavering support and encouragement I have received from many people during the completion my PhD degree.

In particular, I want to express my deepest appreciation to Prof. Ke Xu, for being an ideal advisor. His clear logic and brilliant ideas are always admirable as a scientist, and our discussion always inspired me to break through the challenges I faced along the research. Not only as an academic mentor, he is a wonderful person and has been supportive in every aspect of the life in and outside the research group. Altogether, his guidance and support were invaluable in my academic career.

I am also thankful to my research colleagues Dr. Seonah Moon, Dr. Wan Li, Dr. Kun Chen, Dr. Limin Xiang, Dr. Jeongmin Kim, Dr. Rui Yan, Dr. Changdong He, Yunqi Li, Bowen Wang, Bret Unger, Alex Choi, and Tyler Jephson for their synergistic discussions and immense support; especially to Dr. Seonah Moon who helped me transition into this group and Berkeley.

I would also like to thank the thesis committee, Prof. Stephen R. Leone and Prof. David G. Drubin for being supportive since the qualifying exam. Extra thanks to Prof. Leone for being the first-year advisor and providing guidance until I joined the Xu lab.

I deeply appreciate Jinyoung Seo, Gil Namkoong, Minwoo Bae, Jung-Un Park, and Jeewhan Oh, for being the best friends all the time and at any place. Our conversations were of the most intellectually insightful even though we all majors in different fields of Chemistry, and the most delightful to share every aspect of our lives. I am looking forward to carrying on with synergistic correspondence in the next phases of our career.

Lastly, I am blissful to be a part of my beloved family, who always embraced me and gave unconditional support.

Chapter 1: Introduction

1.1. Single-molecule imaging and localization

1.1.1. Molecular fluorescence

The quantum mechanical structure of molecules is defined by the energy states of electrons: how those energy states (or molecular orbitals) are constructed, and how electrons are distributed among those energy states. The electronic configuration of molecules in the ground state is such that their energy levels are occupied in order of increasing energy. These ground-state molecules can be excited by external stimuli, such as photons. The excitation process takes place in subfemtosecond timescales, so that atomic nuclei cannot follow the relocation of the electron simultaneously, resulting in vibrationally excited molecules (vertical transition, Franck-Condon principle).[1] The vibrational energy soon dissipates into the surroundings (typically, solvent molecules). This thermal relaxation process usually takes picoseconds in the condensed phases, and the resulting electronically excited, vibrationally relaxed state has a nanosecond lifetime before it decays back to the electronic ground state. Such a closed-circuit involving molecule emission is called fluorescence, as the electronic excitation and relaxation accompany the absorption and emission of photons, respectively.

However, molecules cannot absorb or emit just any wavelength of light; their energy states are quantized, and only a photon with an energy that matches the energy difference between two states can cause an electronic transition. Therefore, the wavelengths of the photons corresponding to the fluorescence process are characteristic of the molecule. In the condensed phases, the emission wavelength is always longer than the absorption wavelength as the fluorescence emission takes place after the thermal relaxation. Such properties of molecular fluorescence led to the utilization of those molecules having strong fluorescence (both absorption and emission), dye molecules, in scientific research.[2,3]

1.1.2. Fluorescence microscopy

Scientific studies often rely on visual evidence. Shapes sometimes tell much more than how they look, such as how they work and what they do – the correlation between structures and functions is one of the main strategies to understand rather complex systems. The logic applies the same to the microscopic world: visual clues frequently project properties and mechanisms of cellular machineries and molecules. Among different classes of microscopy, optical microscopy

has been the most popularized tool to interrogate biological systems as visible light is the wavelength window that minimally interferes with cellular components.[4] Specifically, fluorescence optical microscopy is widely adopted for biological research, due to its target specificity.[2,3] The choice of excitation wavelength selectively activates fluorescence dyes, and the emission wavelength differentiated from the excitation wavelength allows background-free, high-sensitivity detection of the target.

However, the tool has a fundamental limitation of spatial resolution. The spatial resolution is a metric of how close two light sources (here, fluorescence target molecule) can be placed while we can still see those as two. Thus, it is the performance of the microscopy that determines how much of the structural details can be obtained. As a point light source through the optical setup of a circular aperture generates the diffraction pattern of the first-order Bessel function of the first kind, the intensity pattern of the point source (point spread function, PSF) is the square of the function (Airy disk).[5] To separately identify two PSFs, the distance must be at least the radius of the first minimum of the Airy disk. This criterion defined by Lord Rayleigh can be described as:

$$\sin \theta_R \approx 1.22 \frac{\lambda}{D} \tag{1.1}$$

where θ_R is the angular resolution at the circular aperture, λ is the wavelength of the light, D is the diameter of the lens. With the approximation that θ_R is small, the microscope resolution is defined by:

$$R = 1.22 \frac{\lambda}{NA_{condenser} + NA_{objective}} = \frac{0.61\lambda}{NA} = \frac{0.61\lambda}{n \sin\theta_L} \tag{1.2}$$

where R is the resolution, NA is the numerical aperture, n is the refractive index of the medium, and θ_L is the half angle of the lens aperture. In epifluorescence microscopy, the light condenser and objective lens are identical, and the resolution of the setup is determined by the NA of the objective lens and wavelength used for imaging. For a typical high-resolution oil immersion lens, NA is around 1.4, therefore the spatial resolution of fluorescence microscopy using visible light (400~700 nm wavelength) is around 200~300 nm. Considering the main (functional) components of biological systems, proteins, are a few nanometers in size, this resolution may limit the usage of fluorescence microscopy to discover biological processes in detail. Moreover, in practical situations, these biological components are often in a state of motion, which can further complicate the microscopy readouts: the convolution of the PSFs over thousands of photons collected along the motion trajectory during the acquisition time.

1.1.3. Single-molecule localization microscopy

Recent decades have witnessed overcoming the resolution limit of optical imaging through engineering microscopy methods. Although different methods have been developed,

namely STORM (Stochastic Optical Reconstruction Microscopy),[6] PALM (PhotoActivated Localization Microscopy),[7] or PAINT (Points Accumulation for Imaging in Nanoscale Topography),[8] they share the same principle to achieve higher spatial resolution: single-molecule localization microscopy (SMLM). Instead of activating all fluorescence molecules as in conventional fluorescence microscopy, SMLM sparsely activates target molecules so that their signals are not overlapping (thus, distinguishable under Rayleigh's criterion). Individual single-molecule signals then are fitted to PSF models (the Bessel function, or more commonly approximated to Gaussian) to precisely define the position of each molecule. By accumulating single-molecule localizations for multiple frames, a super-resolved image of the target can be rendered. Since each microscopy frame is a convolution of photons collected during acquisition time, the lateral localization error of the molecular position is $w_{PSF}/\sqrt{N}$ (w_{PSF} is the width of PSF, N is the number of photons).[9] This term in SMLM is typically 10~30 nm, meaning rendered features in the super-resolution image have lateral precisions in the given scale. The breakthrough of this microscopy technique enabled landmark discoveries of cellular structures and provided crucial insights into understanding their functions.[10–13]

1.2. Single-molecule displacement/diffusivity mapping (SMdM)

1.2.1. Functional single-molecule localization microscopy

Although SMLMs provided unprecedented structural details on structures, yet the information available is limited to spatial coordinates (either 2D or 3D) of fluorescence molecules. Biological systems and their behaviors are rather complex, and essential insights to understand their mechanisms and processes are often embedded in physical and chemical properties alongside the structure. The development of functional SMLM directly aimed to tackle this by decoding single-molecule signals and extracting additional information on top of the spatial coordinate (thus, an additional dimension).[14] The first example of multi-dimensional SMLM is demonstrated by using solvatochromic dyes, of which optical properties are responsive to microscopic local environments such as polarity.[15] Correlative imaging of single-molecule spectra to their positions revealed that different cellular membranes are differentiated by chemical compositions. Alternatively, fluorescence excitation engineering enabled the tracing of fast-diffusing molecules to map out diffusion coefficients correlatively to the super-resolution SMLM images.[16] Diffusivity maps of a protein inside cells showed high coherence with the cellular architectures and that the proteins diffused slowly in sterically hindered parts.

1.2.2. Super-resolution diffusion coefficient mapping

The localization precision of 10~30 nm in SMLM is for static molecules. However, free molecules are continuously in motion so that even large molecules like proteins move hundreds of nanometers in milliseconds. Therefore, the few-millisecond frame exposure time of typical high quantum-yield single-molecule imaging results in extensively blurry single-molecule signals. Moreover, it is highly likely that each molecule captured in one frame will move out of the focus in the next frame (Figure 1a). Single-molecule displacement/diffusivity mapping (SM*d*M) overcame these by introducing tandem stroboscopic excitation, by placing the illumination pulse (typically, a few hundreds of microseconds) in the odd frames near the end of camera acquisition and another pulse in the even frames near the beginning of the acquisition.[16] By reducing the motion blur and thus localization error by shorter illumination (Figure 1b), and by enhancing effective time resolution (down to sub milliseconds) between odd-even frames by pulse timing modulation (Figure 1c), SM*d*M successfully captures freely diffusing molecules and their displacement. The collected step displacements are processed through the maximum-likelihood estimation (MLE) of the 2D-Brownian diffusion, which yields the 2D-diffusion coefficient of the target molecule (Figure 1d). If the sample is spatially heterogeneous, those step displacements can be accumulated on a grid of ~100 nm and generate a super-resolved diffusivity map. Alternatively, when the sample is homogenous, it provides high-throughput diffusivity analysis without spatial binning.
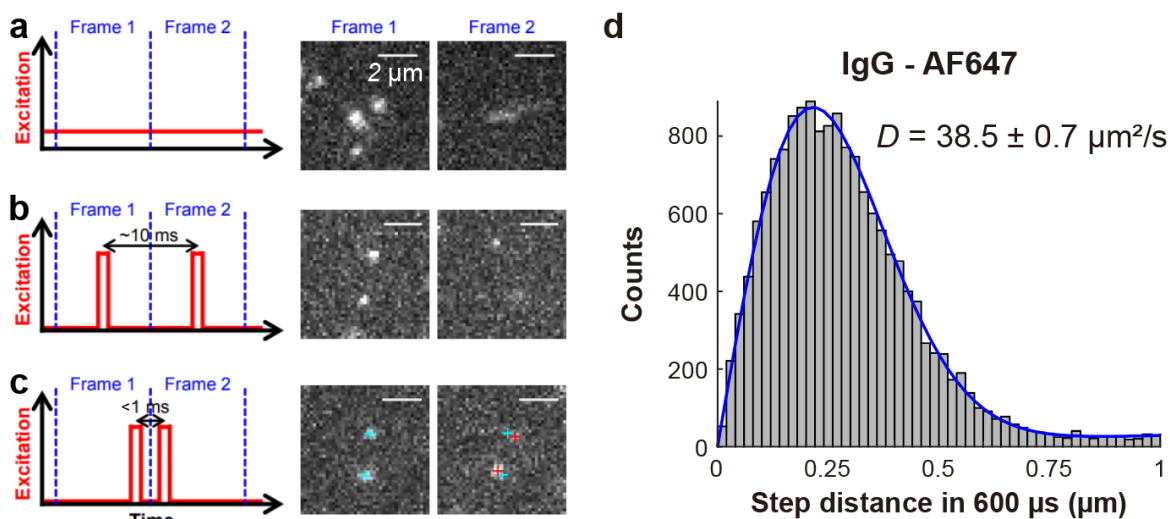
Figure 1. SM*d*M illumination configuration and SM*d*M data from fluorescently labeled protein.
(a) Under conventional illumination of fluorescence microscopy, typical freely diffusing proteins give motion-blurred signals and are highly likely to diffuse out of the focal plane in the consecutive frame. (b) Under stroboscopic illumination, as illumination time is decreased, signals of diffusing single-molecules are less blurred but are still not trackable. (c) When a pair of stroboscopic illumination pulses are placed near the frame-edge, the effective time resolution increases, and freely diffusing molecules are captured in the pair of frames. (d) SM*d*M data and analysis result for IgG labeled with Alexa Fluor 647 (AF647). By repeating the illumination sequence shown in (c) and localizing single-molecule signals, step distances of single-molecules can be calculated between each pair of frames. The collection of step distances (histogram) is processed with the maximum-likelihood estimation (MLE; blue curve) and yields the diffusion coefficient. (a)-(c) modified with permission from Xiang et al.[16] Copyright 2020 Springer Nature.

1.3. Thesis overview

In chapter 2, I present the study on hindered diffusion of proteins in wide ranges of the nanomatrix sizes formed inside synthetic hydrogels. By repurposing the recently popularized expansion microscopy to control the meshwork size of hydrogels,[17,18] we examine the size-dependent suppression of molecular diffusivity in the resultant tuned hydrogel nanomatrices over a wide range of polymer fractions of ~0.14−7 wt %. We show that with a fixed meshwork size, larger molecules exhibit more impeded diffusion and that, for the same molecule, diffusion is progressively more suppressed as the meshwork size is reduced; this effect is more prominent for the larger molecules. Moreover, we show that the meshwork-induced obstruction of diffusion is uncoupled from the suppression of diffusion due to increased solution viscosities. Thus, the two mechanisms, respectively, being diffuser-size-dependent and independent, may separately scale down molecular diffusivity to produce the final diffusion slowdown in complex systems like the cell.

In chapter 3, I present the development of high-resolution diffusivity mapping from single-molecule microscopy using a convolutional neural network. While critical to biological processes, molecular diffusion is difficult to quantify, and spatial mapping of local diffusivity is even more challenging. Here I introduce a machine-learning-enabled approach, pixels-to-diffusivity (Pix2D), to directly extract the diffusion coefficient D from single-molecule images, and consequently enable super-resolved D spatial mapping. Working with single-molecule images recorded at a fixed framerate under typical single-molecule localization microscopy (SMLM) conditions, Pix2D exploits the often undesired yet evident motion blur, *i.e.*, the convolution of single-molecule motion trajectory during the frame recording time with the diffraction-limited point spread function (PSF) of the microscope. Whereas the stochastic nature of diffusion imprints diverse diffusion trajectories to different molecules diffusing at the same given D, we construct a convolutional neural network (CNN) model that takes a stack of single-molecule images as the input and evaluates a D value as the output. We thus validate robust D evaluation and spatial mapping with simulated data, and with experimental data successfully characterize D differences for supported lipid bilayers of different compositions and resolve gel and fluidic phases at the nanoscale.

Publications reproduced in this dissertation are listed below. Permission has been granted by all critical co-authors for the reproduction of the work in the dissertation.

*H. H. Park, A. A. Choi, and K. Xu. "Size-dependent suppression of molecular diffusivity in expandable hydrogels: A single-molecule study." Journal of Physical Chemistry B **127**, (2023): 3333-3339.* Published as part of The Journal of Physical Chemistry virtual special issue "Xiaoliang Sunney Xie Festschrift".

*H. H. Park, B. Wang, S. Moon, T. Jepson, and K. Xu. "Machine-learning-powered extraction of molecular diffusivity from single-molecule images for super-resolution mapping." Communications Biology **6**, (2023): 336.*

*A. A. Choi, H. H. Park, K. Chen, R. Yan, W. Li, and K. Xu, "Displacement Statistics of Unhindered Single Molecules Show no Enhanced Diffusion in Enzymatic Reactions." Journal of American Chemical Society **144**, (2022): 4839-4844.*

Chapter 2: Size-dependent suppression of molecular diffusivity in expandable hydrogels: A single-molecule study

The work in this chapter was conducted in collaboration with Alexander A. Choi and Ke Xu. It is reproduced in part here from ref.[19] and with permission from all coauthors. Copyright 2023 American Chemical Society.

2.1. Introduction

Molecular diffusion underlies vital physical and chemical processes that govern the dynamic behaviors of non-equilibrium systems, including the living cell.[20–24] However, it remains unresolved how and why the intracellular molecular diffusivity scales with the diffuser size.[25–30] Whereas current models often assume that, for molecules $\lesssim 30$ kDa, the intracellular diffusion coefficients D are ~25% of that *in vitro* ($D_{cyto}/D_{water} \sim 0.25$) and that this ratio drops substantially to $\lesssim 0.05$ for molecules $\gtrsim 50$ kDa,[20,24,27] we and collaborators have recently shown that in the mammalian cell, the diffusion of small ($\lesssim 1$ kDa) molecules is only modestly suppressed to $D_{cyto}/D_{water} \sim 0.7$[30] and that, in the bacterial cytoplasm, D_{cyto}/D_{water} drops slowly over the 20−300 kDa range.[29]

Suppressed intracellular diffusion beyond that is expected from the modestly (20−40%) higher viscosity of the cytosol over water[31] is often attributed to obstruction from the nanoscale architectures in the cell. An earlier study has shown that nanomatrices/meshworks formed by cross-linked actin filaments partly recapitulate the diffuser size-dependent slowdown of diffusion, so that at 8 mg/mL (~0.8 wt %) actin, substantial suppressions of D are observed for large DNA molecules.[26] In contrast, no diffuser size-dependent diffusion slowdown is observed with alternative crowding agents such as cytosol or Ficoll-70 polymer solutions,[26] thus emphasizing the importance of cross-linked meshworks, *i.e.*, hydrogels, in the size-dependent obstruction of the diffusion of large molecules. Apart from providing a valuable platform to understand obstructed diffusion, molecular diffusion in hydrogels also plays a vital role in diverse biomedical, chemical, and material applications ranging from drug delivery to separation science.[32–35] Recent years have seen increased interest in examining the diffusion and dynamics of biomolecules and particles in synthetic hydrogels with modern microscopy tools.[33,36–38] However, as each study only tests a few polymer conditions defined by the starting monomer concentrations, they do not provide a complete picture of how the evolution of the meshwork size gives rise to transitions between unimpeded and impeded diffusions. Varying the starting monomer concentrations may further affect the polymerization kinetics and lead to altered microscopic structures beyond simple rescaling of the meshwork size.[39] Thus, it remains a challenge to elucidate how the meshwork size itself controls obstructed diffusion.

In this work, we achieve continuous fine-tuning of the hydrogel nanomatrix meshwork size by borrowing the recent success of expandable hydrogels with high-resolution microscopy,[17,18] including single-molecule and super-resolution microscopy applications.[40–43] By starting with the same monomer concentrations for polymerization and then expanding the resultant hydrogel in a different way, this approach leaves the geometric expansion of meshwork size as the only variable. Integrating our recent development of single-molecule displacement/diffusivity mapping (SMdM),[16,30,44,45] which measures D with high fidelity *via* stroboscopic-illumination-enabled wide-field detection of diffusing single molecules,[46,47] we quantify diffusion-hindering effects in this controllably tuned system. We thus show that under the same hydrogel expansion condition and hence a constant meshwork size, increasingly impeded diffusion occurs for the larger molecules. By fine-tuning the expansion ratio to achieve a wide range of polymer fractions of ~0.14−7 wt %, we then show that for the same molecule, diffusion is progressively more suppressed with reduced meshwork sizes, and that this effect is more prominent for the larger molecules. Moreover, we show that the meshwork-induced obstruction of diffusion is uncoupled from diffusion suppressions due to increased solution viscosity, so the two mechanisms may separately scale down D to produce the final diffusion slowdown.

2.2. Results and discussions

2.2.1. Controllable expansion of the hydrogel

Expansion microscopy[17,18] starts by embedding a (biological) sample in a swellable ionic hydrogel[48,49] of cross-linked poly(acrylamide-*co*-sodium acrylate). Upon hydration, the hydrogel expands isotropically owing to the repulsive charges on the acrylate residues on the polymer chain. Whereas most expansion-microscopy applications use the maximal expansion (~4.5× in each dimension; ~100× in volume) to enlarge structural details, we reason that this system may be repurposed to generate continuously tunable matrix pore sizes and polymer fractions in the final hydrogel, ideal for elucidating the size-dependent diffusion properties of macro(bio)molecules (Figure 2 and Figure 3a).

Thus, starting with a fixed total amount (1.25 M; 8.9 wt %) of acrylamide and sodium acrylate monomers and the same amount (0.8 mol % of monomers) of the crosslinker *N,N'*-methylenebisacrylamide (MBAA), we varied the sodium acrylate fraction to generate hydrogels of different expansibilities. Expansion factors, as defined by the length ratios of the hydrogel after and before the expansion (Figure 2), were thus attained in the range of 1.1−4 (Figure 3b; left *y*-axis), hence ~7−0.14 wt % polymer fractions in the expanded gel (Figure 3b; right *y*-axis). Higher expansion factors were obtained with increased sodium acrylate fractions, and the expansion factor could be further fine-tuned in a reversible fashion by adjusting the solution ionic strength (Figure 4).
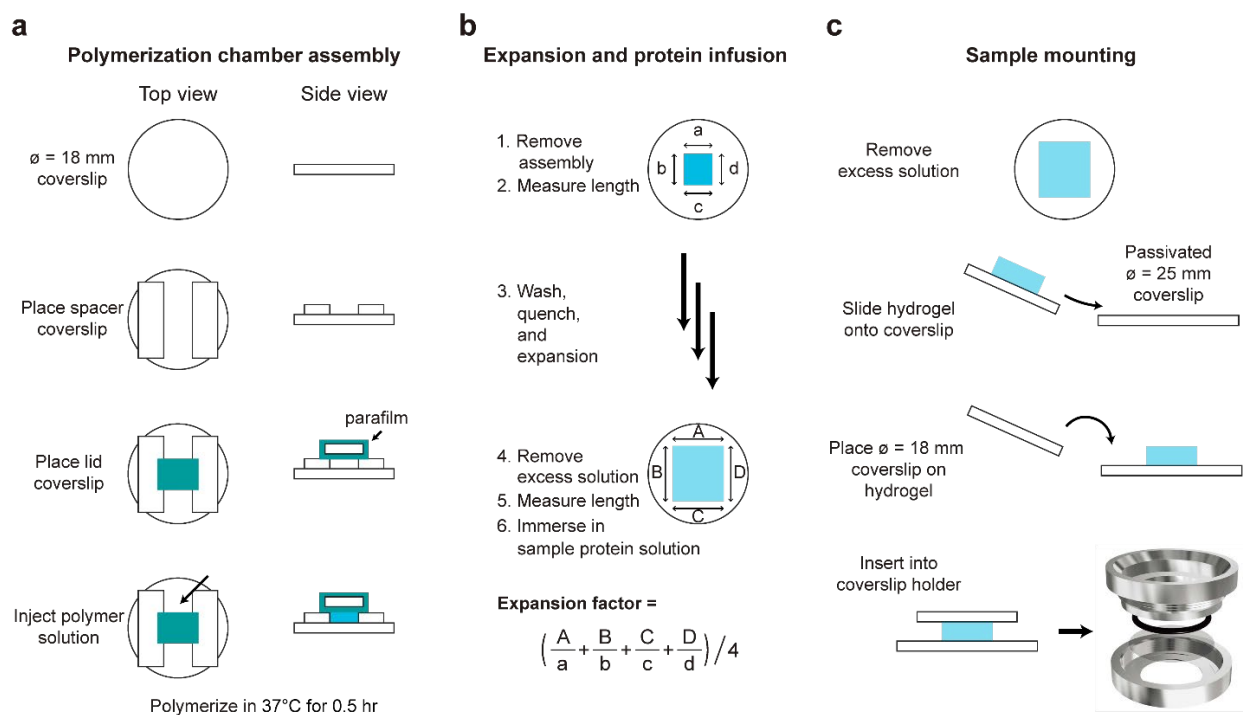
Figure 2. Schematics of the sample-preparation workflow.
(a) Hydrogel is polymerized in a chamber assembled from coverslips. Two small pieces of spacer coverslips were placed on an 18-mm diameter round coverslip at an ~4 mm separation. A small piece of parafilm-wrapped coverslip was used as the top lid of the chamber. 5-10 µL of polymerization mixture is injected into the cavity of the assembly right after TEMED and APS are added. Hydrogel polymerization is completed in a 37°C humidified incubator for 30 min. (b) The polymerization chamber is then disassembled. The dimensions of the resultant hydrogel are measured, and the hydrogel is next washed, quenched, expanded, and infused with the target molecule. Edge lengths of the expanded hydrogel are remeasured, and the expansion factor is calculated. (c) After the excess sample solution is removed, the hydrogel is transferred onto a BSA-passivated 25-mm diameter coverslip and mounted for SMdM.

To characterize molecular diffusion in the hydrogels, we integrated our recently developed SMdM.[16,44,45] In SMdM, fast-diffusing single molecules are imaged in the wide-field by reducing motion blur *via* stroboscopic excitation.[46,47] The stroboscopic pulses are applied in tandem across odd−even camera frames at short time separations of Δt <1 ms (Figure 3c), thus allowing for the determination of single-molecule displacements in the Δt time window. By continuously running this tandem stroboscopic excitation scheme at 110 frames per second, we thus accumulated the transient displacements of >10^4 single molecules (Figure 3d,e) across the camera frame in ~1 min. Fitting the resultant displacement distributions to a random-walk model (Materials and Methods) yielded diffusion coefficient D with <±3% brackets at 95% confidence intervals (Figure 3d,e). We thus found, for example, the diffusion coefficient of the 67 kDa protein bovine serum albumin (BSA) inside a hydrogel expanded in the phosphate-buffered saline (PBS) by a factor of 1.73× (5.2× volume expansion; 1.7 wt % final polymer content) was 52% of that measured in PBS itself (Figure 3d,e).
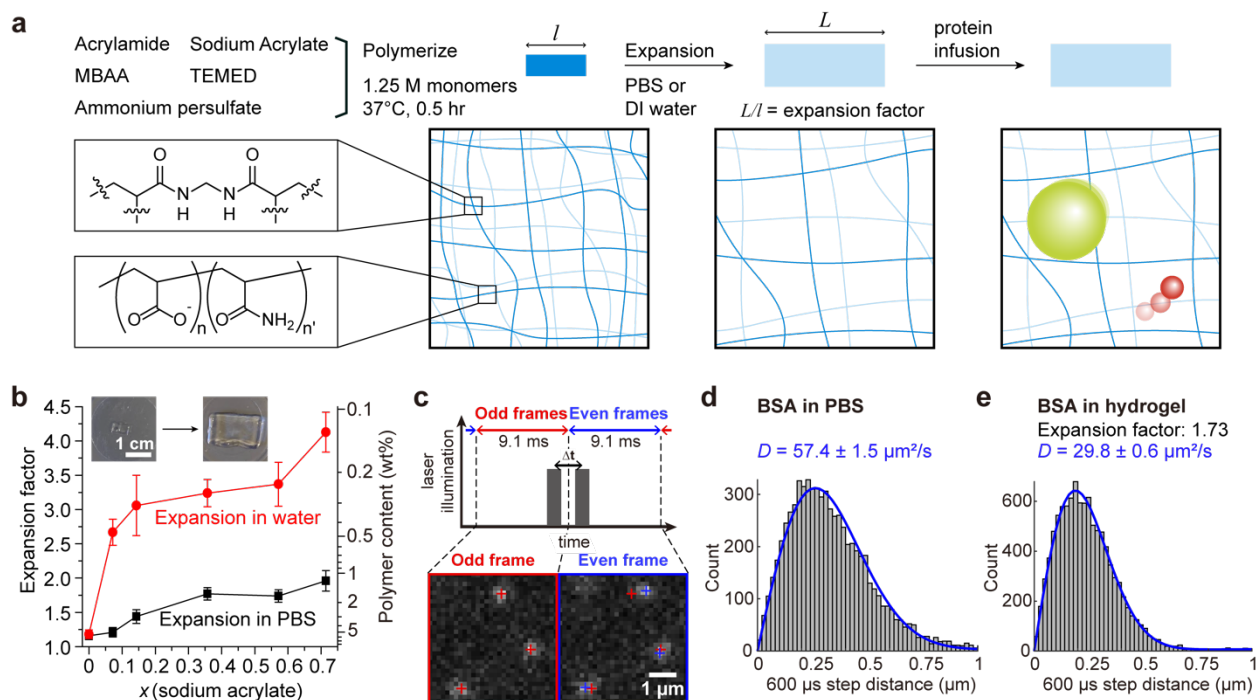
Figure 3. Controlled expansion of hydrogels for the SMdM quantification of molecular diffusivity.
(a) Schematic: *N,N'*-methylenebisacrylamide (MBAA)-crosslinked copolymerization of acrylamide and sodium acrylate generates a hydrogel network that expands isotropically in aqueous solutions. The degree of expansion is controlled by the sodium acrylate fraction and the ionic strength of the solution, hence tunable nanomatrix pore sizes for examining size-dependent molecular diffusion. (b) Measured expansion factor (left y-axis), as defined by the length ratio of the hydrogel after and before the expansion, and corresponding polymer wt% content of the expanded hydrogel (right y-axis), for hydrogels polymerized from different mole fractions of sodium acrylate and then expanded in the PBS (black) or water (red). Error bars: standard deviations between different runs. Inset: photos of a sample before and after 2.98x expansion in water. (c) SMdM: paired stroboscopic illumination pulses across tandem camera frames enable the detection of single-molecule displacements over a short time window, *e.g.*, Δt = 600 μs for the example images shown for Cy3B-labeled BSA diffusing in an expanded hydrogel. The paired excitation scheme is repeated ~6,000 times to establish statistics. (d,e) Example distributions of 600-μs single-molecule displacements for Cy3B-labeled BSA freely diffusing in PBS (d) vs. in a hydrogel expanded by 1.72x in PBS (e). Blue curves: Maximum likelihood estimation (MLE) with our diffusion model, yielding D = 57.4±1.5 and 29.8 ± 0.6 μm²/s (95% confidence intervals), respectively.

To examine how the polymer meshwork may differently suppress the diffusion of molecules of varied sizes, we quantified the diffusion coefficient D of the 0.6 kDa free dye Cy3B and dye-labeled proteins, the 14 kDa ribonuclease A (RNase A), the 67 kDa BSA, and the 150 kDa immunoglobulin G (IgG), in PBS and in hydrogels of two contrasting expansion factors. Here we chose four highly water-soluble targets that substantially differ from each other in size, so that the size effect may stand out over other potential factors as molecular shape and hydrophobicity. For diffusion in PBS, SMdM yielded D values in the range of 40−350 μm²/s that dropped monotonically with the molecular weight M (Figure 5), comparable to our previous results[45]

10

affirming the $D \sim M^{-1/3}$ model of Young-Carroad-Bell,[50] and we obtained similar D values with $\Delta t = 400$ and 600 µs (Figure 5).
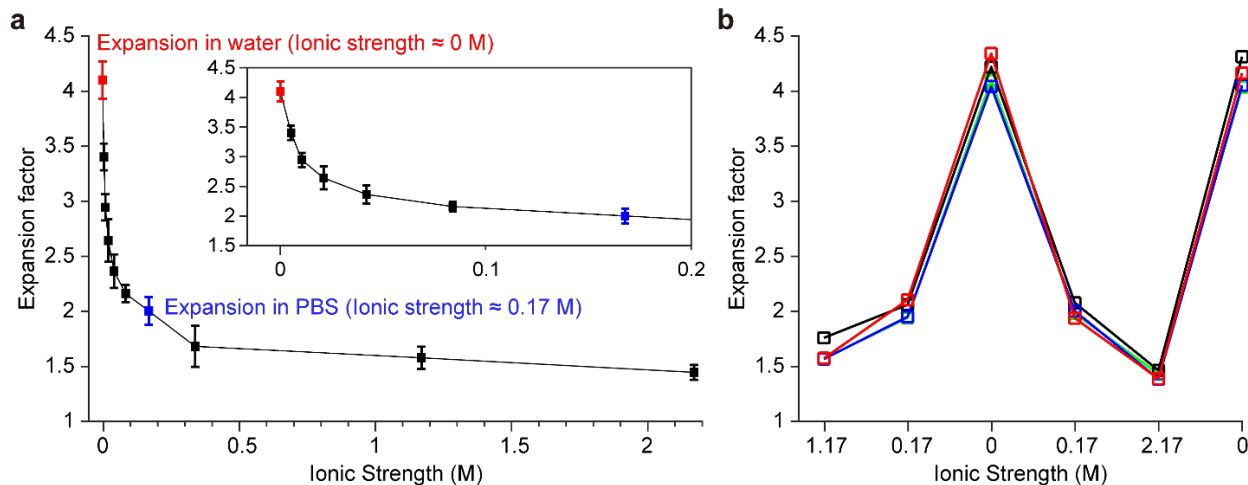
Figure 4. Tuning the hydrogel expansion factor through the solution ionic strength.
(a) Measured expansion factor, as defined by the length ratio of the hydrogel after and before the expansion, for hydrogels polymerized with 0.71 mole fraction of sodium acrylate and expanded in solutions of different ionic strengths. Error bars: standard deviations between different samples. Inset: zoom-in of the low ionic strength part. (b) Reversible modulation of hydrogel expansion by varying the solution ionic strength. Four hydrogel samples polymerized with 0.71 mole fraction of sodium acrylate were sequentially equilibrated with solutions of different ionic strengths, under which conditions the hydrogels expanded and shrank to different expansion factors in a reversible fashion.

2.2.2. Hindered diffusion of single-molecules in expandable hydrogels

For in-gel diffusion, SMdM indicated that in hydrogels expanded by 3.31 ± 0.30 in water (36× volume expansion; 0.24 wt % final polymer content), D of all diffusers remained largely unaffected, *i.e.*, $D_{gel}/D_{PBS} \sim 1$ (Figure 6a). In contrast, in hydrogels expanded by 1.66 ± 0.14 in PBS (4.6× volume expansion; 1.9 wt % final polymer content), SMdM unveiled a striking size-dependent suppression of diffusion (Figure 6a). Whereas the diffusivity of the 0.6 kDa Cy3B was only slightly impeded to $91 \pm 3\%$ of its value in PBS, steady drops to $78 \pm 8\%$, $60 \pm 10\%$, and $50 \pm 10\%$ of the PBS values were, respectively, found for the increasingly larger RNase A, BSA, and IgG. Examination of the SMdM-recorded transient single-molecule displacements yielded good fits to our random walk model (Figure 6b,c), suggesting normal diffusion of the differently impeded proteins at the temporal (~500 µs) and length (~300 nm) scales of our experiments. This marked size-dependent depression of diffusion is consistent with a model in which as we reduce the mesh size of our hydrogel system to the few-nanometer scale,[51] larger molecules are more affected by the nanomatrix (schematics in Figure 3a).
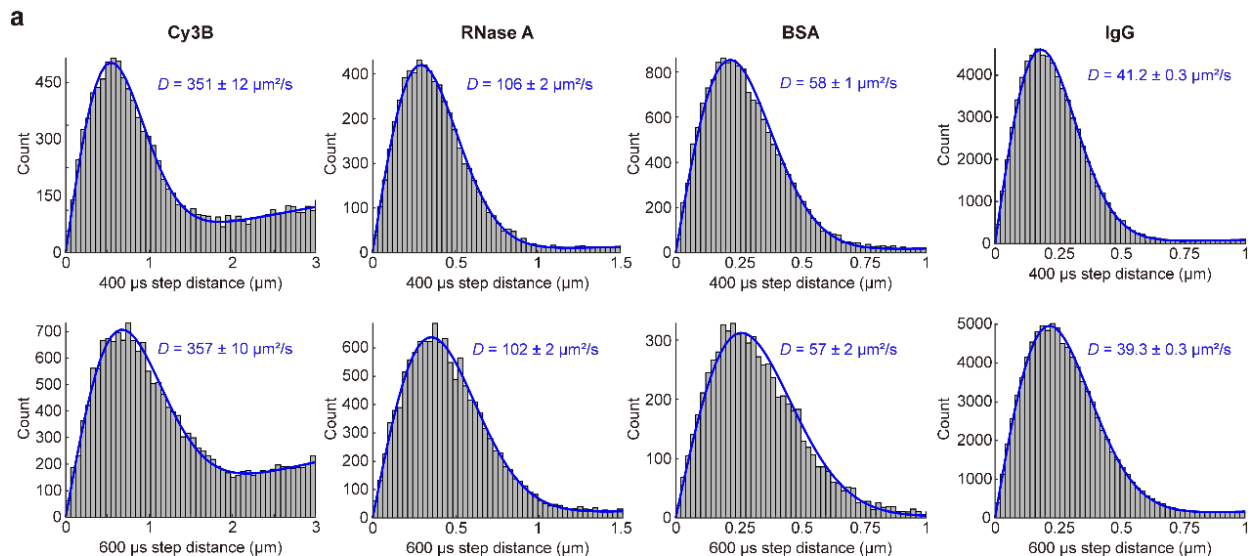
Figure 5. SM*d*M results in PBS of four molecules used in this work.

(a) Histograms showing the distributions of cumulated step distances in SM*d*M carried out at different time separations Δt of 400 and 600 µs, for Cy3B, ribonuclease A (RNase A), bovine serum albumin (BSA), and immunoglobulin G (IgG). Blue curves: MLE results, with the resultant 95% confidence intervals of D values marked in each plot. (b) Molecular weight M and SM*d*M-determined D values of the four diffusers. Means and standard deviations were calculated from multiple SM*d*M measurements. The mean values are used as references to calculate the relative diffusivities in this work.

We next focused on Cy3B and BSA as representative small and macromolecules, and fine-tuned the hydrogel expansion factor to examine how their diffusion transits from unimpeded to impeded as the meshwork size is gradually reduced. SM*d*M showed that for the 0.6 kDa small molecule Cy3B (Figure 7a,b), only mild drops in D occurred when the linear expansion factor was reduced to <2 (8× volume expansion; 1.1 wt % polymer content), with the D value lowering to~85% of that in PBS in the limit of expansion factors of 1.1−1.2 (~6 wt % polymer content). In contrast, for the 67 kDa BSA protein (Figure 7a,c), SM*d*M unveiled notable decreases in D for expansion factors <3 (27× volume expansion; 0.33 wt % polymer content), and D dropped to 50−70% and ~30% of that in PBS at expansion factors of ~2 (1.1 wt % polymer content) and 1.1−1.2 (~6 wt % polymer content), respectively.
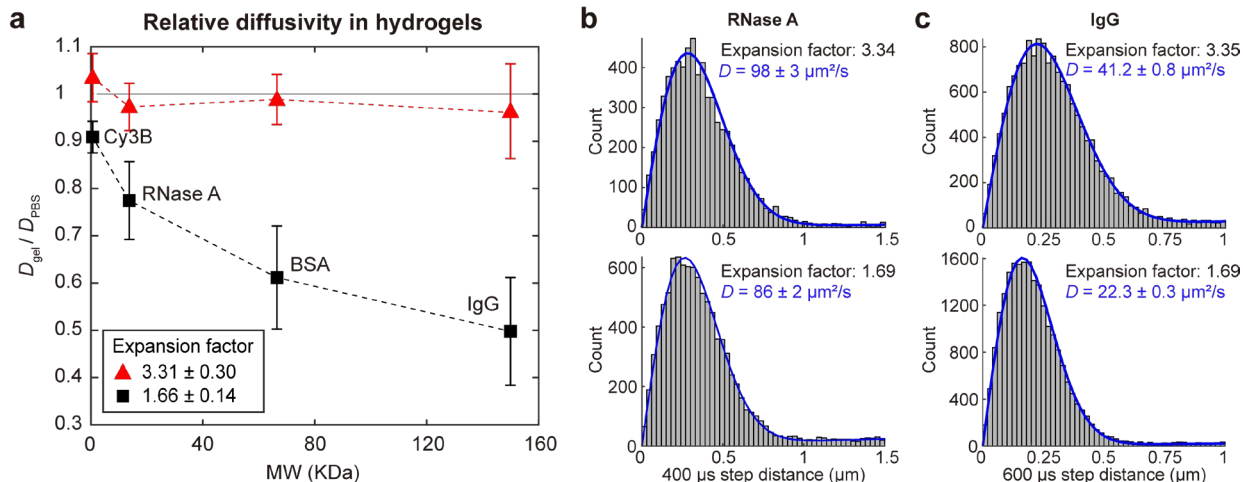
Figure 6. Molecular size-dependent suppression of diffusivity in differently expanded hydrogels.

(a) SM*d*M-determined in-gel diffusion coefficient D relative to that in the PBS buffer for the 0.6 kDa free dye Cy3B and dye-labeled proteins, the 14 kDa ribonuclease A (RNase A), 67 kDa bovine serum albumin (BSA), and 150 kDa immunoglobulin G (IgG), in hydrogels expanded by 1.66±0.14 in PBS (black) vs. by 3.31±0.30 in water (red). Error bars: standard deviations from ~8 hydrogels for each condition. (b,c) Example histograms of SM*d*M single-molecule displacements for RNase A (b) and IgG (c) under the two expansion conditions. Blue curves: MLE results, with the resultant 95% confidence intervals of D values marked in each plot.
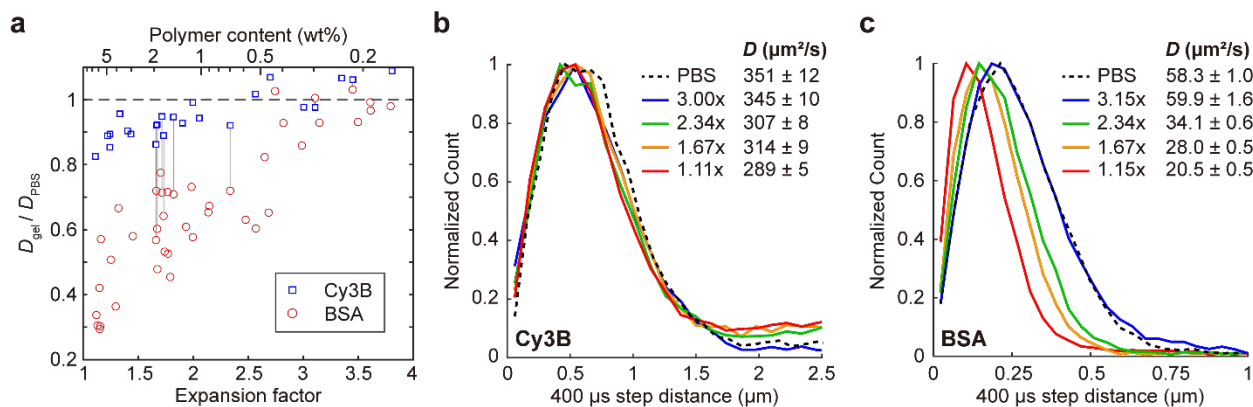
Figure 7. Contrasting diffusivity scaling behaviors in expanded hydrogels for Cy3B and BSA.

(a) The SMdM-determined in-gel diffusion coefficient D relative to that in the PBS buffer for the 0.6 kDa dye Cy3B (blue) and the 67 kDa protein BSA (red), in different hydrogel samples at varied expansion factors (bottom x-axis) and hence polymer contents (top x-axis). Vertical lines connect paired data, in which the diffusion of AF647-labeled BSA and Cy3B were sequentially measured through 2-color SMdM in the same gel sample. (b) Normalized count distributions of the SMdM-measured 400 μs single-molecule displacements for Cy3B diffusing in PBS (dash line) and in four hydrogel samples of different expansion factors (solid lines), with respective MLE results shown in the legend as 95% confidence intervals. (c) Similar to (b) but for the diffusion of BSA.

13

To further substantiate the contrasting scaling behaviors of Cy3B and BSA, in several gel samples we examined the diffusion of both molecules by performing two-color SM*d*M, using the spectrally distinct Alexa Fluor 647 (AF647) to label BSA (Figure 8). The sequentially acquired SM*d*M data in the two color channels (connected by vertical lines in Figure 7a) thus confirmed in the same samples distinct relative *D* values over PBS, with the diffusion of BSA being substantially more suppressed. Together, these results indicate that the diffusion of the 67 kDa BSA molecule is progressively more impaired as the hydrogel mesh size is continuously reduced to reach polymer contents of >0.33 wt %, whereas the 0.6 kDa Cy3B does not quite "sense" the existence of the polymer nanomatrix even at much higher polymer contents.
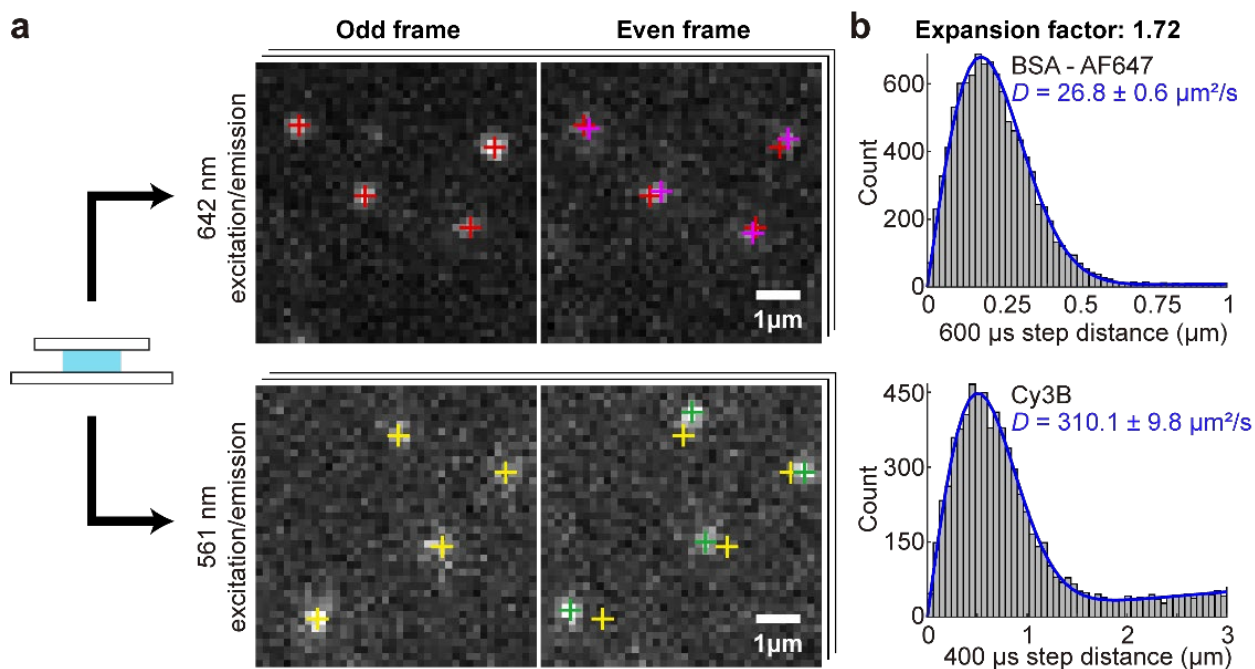
Figure 8. Two-color SM*d*M for analyzing the diffusivity of two molecular species in the same hydrogel.
(a) Example paired single-molecule images between odd and even frames, from SM*d*M data sequentially acquired under 642- and 561-nm excitations with corresponding filter sets. The hydrogel sample had an expansion factor of 1.72, and was infused with the 642-excited AF647-labeled BSA and 561-excited Cy3B. Crosses: the super-localized positions of identified single molecules. (b) Distribution of single-molecule displacements from the SM*d*M results of the two color channels, showing contrasting diffusivities of the two diffusers. Blue curves: MLE results, with the resultant 95% confidence intervals of *D* values marked in each plot.

2.2.3. Independent diffusion hindrances from solution viscosity and nanomatrix

As intracellular diffusion is suppressed by both the nanoscale architecture of the cell and the 20− 40% higher viscosity of the cytosol over water,[31] we next probed, with our expandable

hydrogel system, whether the two effects would independently modulate the diffusion of small and macromolecules. To this end, we thickened the solution by adding the inert small molecule glycerol.[52,53] SMdM showed that in an 18 wt % glycerol solution, the D values of Cy3B and BSA dropped to 217 and 35 μm²/s (dash-dot curves in Figure 9b,c), respectively, corresponding to 62% and 60% of that in PBS (dash curves in Figure 9b,c). These diffuser size-insensitive values match that predicted (60%) through scaling the known glycerol concentration-dependent viscosity.[52,53]

We next examined the diffusion of both molecules in our hydrogel system expanded in the presence of 18 wt % of glycerol. Interestingly, as we plotted the SMdM-determined relative D values over that in the 18 wt % glycerol solution, we observed similar expansion-factor-dependent D scaling as hydrogels expanded in PBS (Figure 9a). Thus, obstruction of diffusion due to the hydrogel nanomatrix is uncoupled from diffusion suppressions due to higher solution viscosities, and the two factors may each separately scale down the D values to produce the final diffusion slowdown.
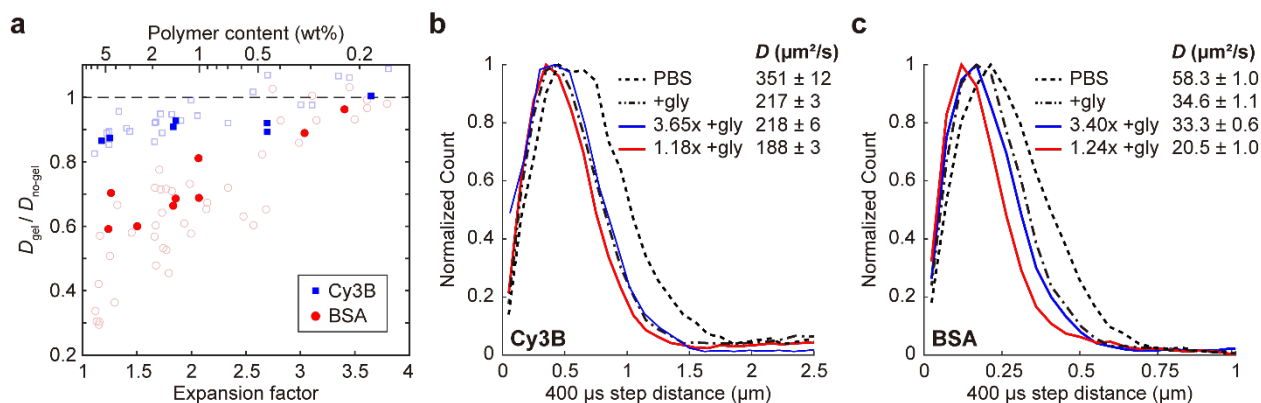
Figure 9. Uncoupled diffusion suppressions by the solution viscosity and by the hydrogel nanomatrix. (a) Solid symbols: the SMdM-determined in-gel diffusion coefficient D of Cy3B (blue) and BSA (red), in hydrogels expanded at different expansion factors (bottom x-axis) and hence polymer contents (top x-axis) in solutions containing 18 wt% glycerol, relative to that in the 18 wt% glycerol solution. Hollow symbols: reproduced from Figure 7a for in-gel D relative to no-gel for hydrogels expanded in PBS. (b) Normalized count distributions of the SMdM-measured 400 μs single-molecule displacements for Cy3B diffusing in PBS (dash line), in the 18 wt% glycerol solution (dash-dot line), and in two hydrogels of different expansion factors in 18 wt% glycerol solutions (solid lines). MLE results are shown as 95% confidence intervals in the legend. (c) Similar to (b) but for the diffusion of BSA.

2.3. Conclusion

Together, by repurposing the recently popularized expansion microscopy to achieve controlled tuning of the hydrogel meshwork size, we examined the in-gel diffusion of small and

macromolecules over a wide range of polymer fractions of ~0.14−7 wt %. Through SMdM single-molecule measurements, we thus showed that with a constant meshwork size, larger molecules exhibited more impeded diffusion, and that for the same molecule, diffusion is progressively more suppressed as the meshwork size was reduced, and this effect was more prominent for the larger molecules. Whereas similar trends have been reported with hydrogels prepared from discrete initial monomer concentrations,[37,38,54] our approach both ensured the geometric expansion of meshwork size as the only variable between different samples and achieved continuous fine-tuning of the meshwork size. Moreover, by thickening the solution while conserving the hydrogel expansion factors, we showed that the meshwork-induced obstruction of diffusion is uncoupled from the suppression of diffusion from increased solution viscosities.

In complex systems like the cell, the two mechanisms, respectively being diffuser-size dependent and independent, should separately scale down D to produce the final diffusion slowdown. On this discussion, our observation that the formal factor caused minimal slowdowns for Cy3B, even in the limit of low expansion factors where substantial diffusion obstruction was observed for macromolecules, echoes our recent finding that the intracellular D of small molecules is only modestly depressed to ~70% of that in water by the slightly higher viscosity of the cytosol.[30] Meanwhile, the demonstrated unconventional use of expandable hydrogel and expansion microscopy for physical-parameter tuning provides an appealing path toward the future development of manipulation and measurement tools.

2.4. Materials and methods

Preparation of fluorescence dye-labeled proteins

Ribonuclease (RNase) A (Sigma, R5500) and bovine serum albumin (BSA, Sigma, A3059) were labeled with Cy3B or Alexa Fluor 647 (AF647) via NHS (*N*-hydroxysuccinimide) ester conjugation. Cy3B-NHS (Cytiva, PA63101) or AF647-NHS (ThermoFisher, A37573) were mixed with protein in 0.1 M NaHCO$_3$ at a 10:1 dye-to-protein ratio, incubated at room temperature for 1.5 hr, are then purified with 3k and 10k MWCO centrifugal filters, respectively (Millipore, UFC500396 and UFC501096). The resultant dye-to-protein ratios were 0.5-1.5, as determined with a NanoDrop 2000c spectrometer (ThermoFisher). Dye-labeled RNase A was further treated with sulfo-NHS-acetate (ThermoFisher, 26777) to cap the excessive lysines. For immunoglobulin G (IgG), a commercial AF647-labeled goat anti-mouse secondary antibody (ThermoFisher, A21236) was used.

Preparation of expandable hydrogel

Sodium acrylate (Sigma, 48220), acrylamide (Sigma, A9099), *N,N'*-methylenebisacrylamide (MBAA, Sigma, M7279), *N,N,N',N'*-tetramethyl ethylenediamine (TEMED, Sigma, T7024) and ammonium persulfate (APS, Sigma, A3678) were prepared as stock solutions of 0.38, 0.5, 0.02, 0.1, and 0.1 g/mL in water, respectively. Monomer mixture solutions were prepared from the stock solutions to 1.25 M total concentrations with varied sodium acrylate and acrylamide mole fractions and a fixed 0.8% mole fraction of MBAA. To initiate polymerization, TEMED and APS were added, both to 0.2% wt. in the final mixture, and the mixture was quickly injected into a gel-formation chamber (Figure 2) adopted and modified from standardized expansion-microscopy protocols.[55,56] The assembly was placed in a 37 °C humidified incubator for 30 min. The chamber was dissembled, and the lengths of the four edges of the resultant hydrogel were measured. Each hydrogel was then expanded in a solution of a fixed ionic strength for 10 min, followed by a racial-quenching solution of the same ionic strength but with the addition of 1 mM of 4-hydroxy-TEMPO (Sigma, 176141) for 30 min, and then the same expanding solution without 4-hydroxy-TEMPO for 10 min. Ionic strengths lower or higher than that of phosphate-buffered saline (PBS; 14190144, Gibco) (160 mM) were prepared by diluting PBS with Milli-Q water or by adding NaCl to PBS, respectively. To infuse dyes and dye-labeled proteins, the hydrogel was immersed in the same expanding solution with the addition of 150−300 pM of the fluorescent probe for 10−20 min. The dimensions of the hydrogel were remeasured, and the averaged length ratio over that before the expansion was taken as the expansion factor. Excess solution was removed, and the hydrogel was transferred onto a BSA-passivated 25-mm diameter #1.5 coverslip, and mounted into the coverslip holder (ThermoFisher, A7816). Coverslip passivation was done through the sequential sonication in acetone and Milli-Q water for 5 min each, treating with 10 mg/mL BSA in PBS for 30 min, rinsing with Milli-Q water, and drying with N_2 gas.

Optical setup

SM*d*M was performed on a Nikon Ti-E inverted fluorescence microscope, as described previously.[16,44,45] A 561 nm laser (OBIS 561 LS, Coherent, 165 mW) and a 642 nm laser (Stradus 642, Vortran, 110 mW) were focused at the back focal plane of an oil-immersion objective lens (Nikon CFI Plan Apochromat λ 100×, numerical aperture 1.45). A translation stage shifted the laser beams toward the edge of the objective lens to reach the sample at an incidence angle slightly below the critical angle of the coverslip-hydrogel interface, thus illuminating a few micrometers into the hydrogel. Single-molecule images were collected 1.5−2 μm away from the coverslip surface. Fluorescence emission under 561 nm excitation was filtered by long-pass (ET575lp, Chroma) and band-pass (ET605/70m, Chroma) filters. Fluorescence emission under 642 nm excitation was filtered by long-pass (ET655lp, Chroma) and band-pass (ET705/100m, Chroma) filters. Wide-field single-molecule images were collected at 110 frames per second for 5,000-8,000 frames with an EM-CCD camera (iXon Ultra 897, Andor). For SM*d*M pulse control, the excitation lasers were modulated by a multifunctional input/output board (PCI-6733, National Instruments), which read the EMCCD camera exposure output signal to enable pulse-frame synchronization. Tandem laser pulse sequences were applied at fixed center-to-center separations Δt of 400 or 600 μs, with corresponding pulse durations set at 200 and 400 μs, respectively.

Chapter 3: Machine-learning-powered extraction of molecular diffusivity from single-molecule images for super-resolution mapping

The work in this chapter was conducted in collaboration with Bowen Wang, Suhong Moon, Tyler Jepson, and Ke Xu. It is reproduced in part here from ref.[57] and with permission from all coauthors. Copyright 2023 Park et al. under the terms of the Creative Commons Attribution License, which permits unrestricted use and redistribution provided that the original author and source are credited.

3.1. Introduction

Molecular diffusion underlies vital cellular processes.[20,58–60] The diffusion coefficient D, a metric of how fast molecules diffuse, is a function of both the molecular size and intracellular parameters such as viscosity and intermolecular interactions. This correlation between diffusion and intracellular parameters has led to the use of D as a reporter of intracellular (micro)environments to correlate dynamic properties with structures.

Many fluorescence microscopy techniques have been developed to probe diffusion at different spatiotemporal scales. Traditional approaches such as fluorescence recovery after photobleaching (FRAP)[60] and fluorescence correlation spectroscopy (FCS)[59,61–64] offer limited capabilities for spatial mapping, and they often encounter background and calibration challenges when applied to biological samples. Single-particle tracking (SPT)[65–68,22] provides high spatial-resolution measurements for molecular diffusion, and with recent developments integrating photoactivation and related concepts from single-molecule localization microscopy (SMLM), has substantially increased the density of single molecules that can be tracked in the sample.[65,67] However, SPT aims at obtaining long single-particle tracks, from which the D value of each particle is calculated. The need to track the same particle over many consecutive frames limits the application to photostable particles consistently bound to the target, *e.g.*, lipid membranes, while also limiting the spatial mapping capabilities.[65,67,69]

We recently developed single-molecule displacement/diffusivity mapping (SM*d*M), which focuses on detecting the transient motion/velocity of single molecules across tandem camera frames under frame-synchronized stroboscopic illumination.[16] By eliminating the need to track long trajectories, the approach works well for unbound fluorescent proteins in the cell[16] and dye molecules dynamically entering and leaving lipid membranes.[44] The accumulation of many transient displacements over different frames further enables local statistics[14] and D mapping. The need for frame-synchronized stroboscopic illumination, however, limits the adaptation of this

technique. Moreover, each molecule needs to be successfully captured in two consecutive frames and correctly paired to yield a useful measurement, limiting the possible throughput.

Here we report a strategy, pixels-to-diffusivity (Pix2D), to directly extract D values from single-molecule images recorded under typical SMLM conditions. We reason that for diffusing molecules, images recorded at a fixed camera framerate are the convolution of their motion trajectories and the microscope point spread function (PSF), with the faster-moving molecules exhibiting stronger motion blurs. Whereas such information may not directly yield a meaningful D value for each molecule due to the stochastic nature of diffusion, accumulating many molecules over different frames may enable spatial binning for local analysis[14] and thus D mapping at the super-resolution level. Although previous work has extracted D from single-molecule images,[70–72] a global D value is obtained for each sample without spatial mapping, and the model-based fitting approach is susceptible to experimental factors such as camera pixelation effects and backgrounds.

In this work, we seize the rising opportunities of modern machine-learning approaches to directly link single-molecule images to D values without assuming any models, and we further achieve super-resolution mapping. Recent years have witnessed the fast growth of machine learning in single-molecule microscopy,[73] with applications ranging from the enhancement of localization[74–85] and tracking[86–88] to the characterization of diffusive modes and properties.[89–92] In a previous study, we demonstrated the use of neural networks to connect single-molecule images to their color and depth information, thus enabling two-color three-dimensional SMLM.[77] Here we construct a convolutional neural network (CNN) model to connect stacks of single-molecule images to D values. Spatially binning single-molecule images accumulated from many frames further enables local image stacks to be used as inputs for the model to generate D maps at the super-resolution level.
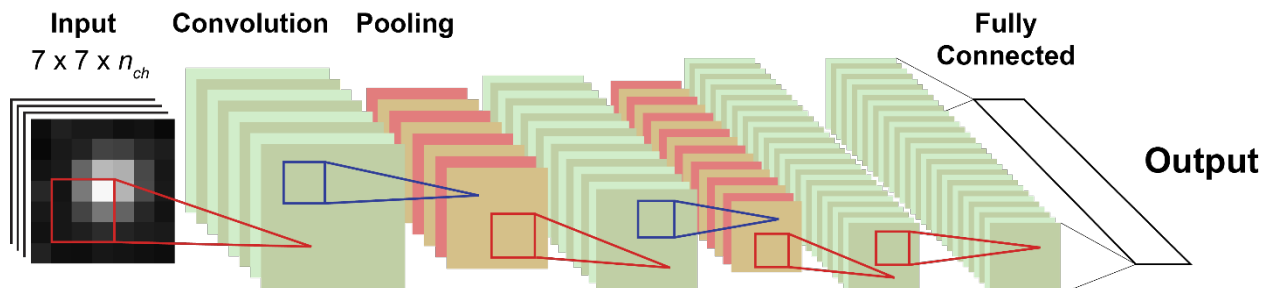
Figure 10. Architecture of the Pix2D convolutional neural network model.

The CNN model processes input through a 3×3 convolution filters of twice the input channel size ($2n_{ch}$), a 2×2 pooling layer applied at stride 2, another 3×3 convolution filters with $4n_{ch}$ channels, another 2×2 pooling layer applied at stride 2, two consecutive 3×3 convolution filters with $8n_{ch}$ channels, followed by a fully connected layer and then final regression layer to the output. The final prediction was computed by a fully connected layer, followed by a regression layer that calculated the MSE losses between the predicted values and the ground truth labels.

3.2. Results and discussions

3.2.1. Construction of diffusivity-mapping CNNs.

We constructed a CNN architecture that maps single-molecule images to D values. As discussed, an individual single-molecule image does not provide a meaningful readout for D. Thus, we built a CNN model that took a stack of uncorrelated single-molecule images as the input and predicted a D value as the output. Following the design principles of ResNet,[93] a seminal work in deep neural network architectures, we designed the CNN model stacking multiple convolutional layers, a fully connected layer, and the final regression layer (Figure 10). Each convolutional building block entailed a convolutional layer with a kernel size of 3, a batch normalization layer,[94] and Swish activation.[95] Whereas ResNet uses the ReLU[96] activation function, we employed the
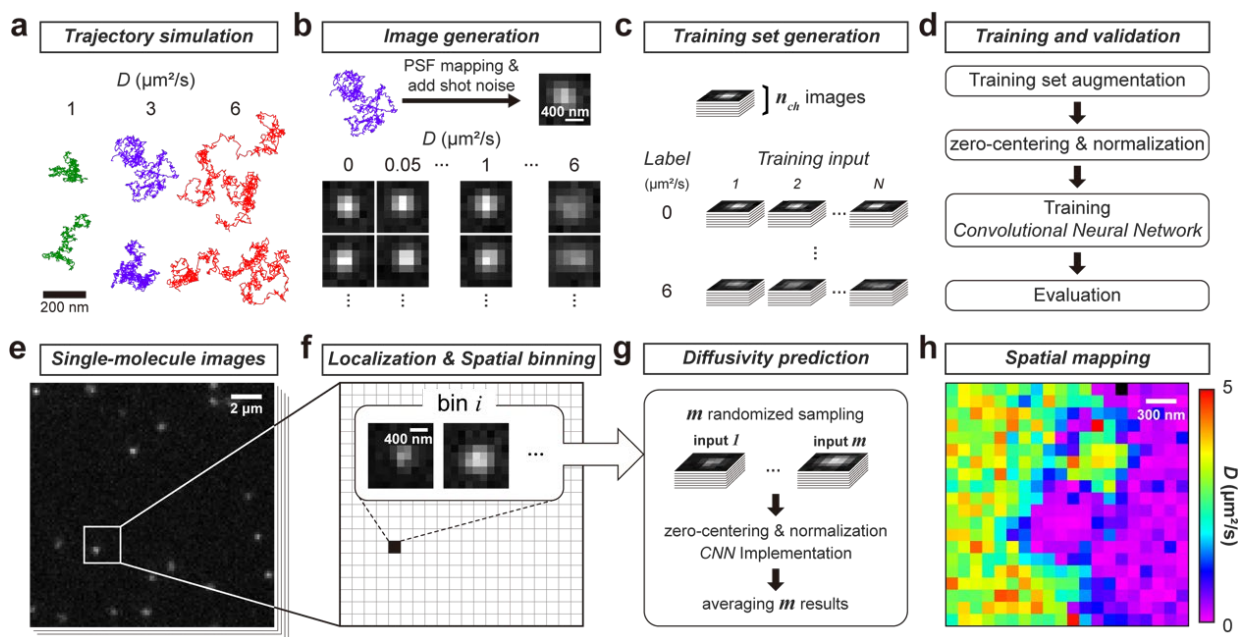
Figure 11. Pix2D CNN training and implementation.
(a) Examples of simulated Brownian trajectories for D = 1, 3, and 5 µm²/s for a camera exposure time of 9 ms. (b) Mapping of simulated trajectories to pixelized images using the microscope point spread function profile and a pixel size of 160 nm. 400 independent trajectories were initially generated for every D value in the range of 0-6 µm²/s at a 0.05 µm²/s spacing. (c) As CNN training input, for each D label, hundreds of stacks of n_{ch} simulated images, each sampled as 7×7 pixels, were initially selected per diffusivity label. (d) The training data were then augmented *via* domain randomization, in which multiple image sets were created through identical processes as in (a)-(c), but with different combinations of noise levels and photon counts. The CNN model was then trained with the augmented data. (e-h) Implementation of Pix2D diffusivity spatial mapping. Single-molecule signals from the raw image sequence were localized and spatially binned with a fixed grid size (f is a zoom-in of the boxed region in e). (g) For each bin, m = 100 permutations of n_{ch} single-molecule images were each fed to the trained model. The resultant m predicted D values were averaged to give the diffusivity of the bin. (h) The results of different spatial bins were color-coded to generate a spatial map.

Swish activation function for our regression task. A relatively shallow CNN model was implemented to avoid overfitting.

Here we focus on diffusion in a two-dimensional system, so that single-molecule motion blurs are not further convoluted with off-focusing. For training, single-molecule images were generated by mapping simulated two-dimensional Brownian trajectories (Figure 11a) to pixelized intensities using the PSF profile of our microscope setup (Figure 11b). To match typical experimental settings, simulations were performed for a pixel size of 160 nm and an exposure time of 9 ms per frame. The input was a stack (n_{ch} channels) of uncorrelated single-molecule images cropped at 7×7 pixels (Figure 11c). Training (Figure 11d) was performed on a dataset augmented with different molecule brightnesses and backgrounds (see below), with each diffusivity label containing hundreds of such stacks as the training inputs (Materials and Methods).

For spatial mapping of diffusivity, single-molecule images (Figure 11e) were first localized in each frame via centroid fitting. A region of interest (ROI) of 7×7 pixels was sampled around the center of each localized molecule, and molecules with overlapping ROIs were discarded. The localized molecules, accumulated from many frames, were then spatially binned onto a fine grid (~100 nm) (Figure 11f), so that each bin had a pool (p^i for bin i) of single-molecule images. For every bin satisfying $p^i > 10$, $m = 100$ inputs, each with the same dimensionality as the training data – thus 100 different $7 \times 7 \times n_{ch}$ arrays – were generated by random sampling from the p^i images for feeding into the model (Figure 11g). The resultant 100 outputs from the model were averaged to yield the diffusivity of the bin. The results of different spatial bins were then color-coded to generate a spatial map (Figure 11h).

3.2.2. Performance of Pix2D.

Figure 12a shows the model prediction results with $n_{ch} = 40$, using evaluation data not included in the training data. To avoid biases due to capping at the upper bound of the training range, here we trained the model with $D = 0$–6 $\mu m^2/s$ data, and applied it to evaluate data generated with D of 0–5 $\mu m^2/s$. Statistics of the Pix2D results on 400 evaluation inputs at each diffusivity yielded averages (Figure 12a, black dots) well following the ground truth (Figure 12a, red line), and the relative errors, %Error = $(E - T)/T \times 100\%$, with E and T respectively being the Pix2D-evaluated and ground-truth D values, showed typical standard deviations of ~12% (Figure 12a shaded areas and Figure 12b).

We next examined how the relative standard error depends on the data size. Comparing the model evaluation results with different n_{ch} and p^i values in the range of 20-160 (Figure 13) indicated that the final precision depends only on the latter, namely, the count of starting single-molecule images. Thus, the choice of n_{ch} was non-critical, and we found the $n_{ch} = 40$ and $m = 100$ combination we used practical. Plotting the relative standard errors as a function of p^i showed a monotonic decrease for an increased single-molecule count (Figure 12c). We have recently shown

21
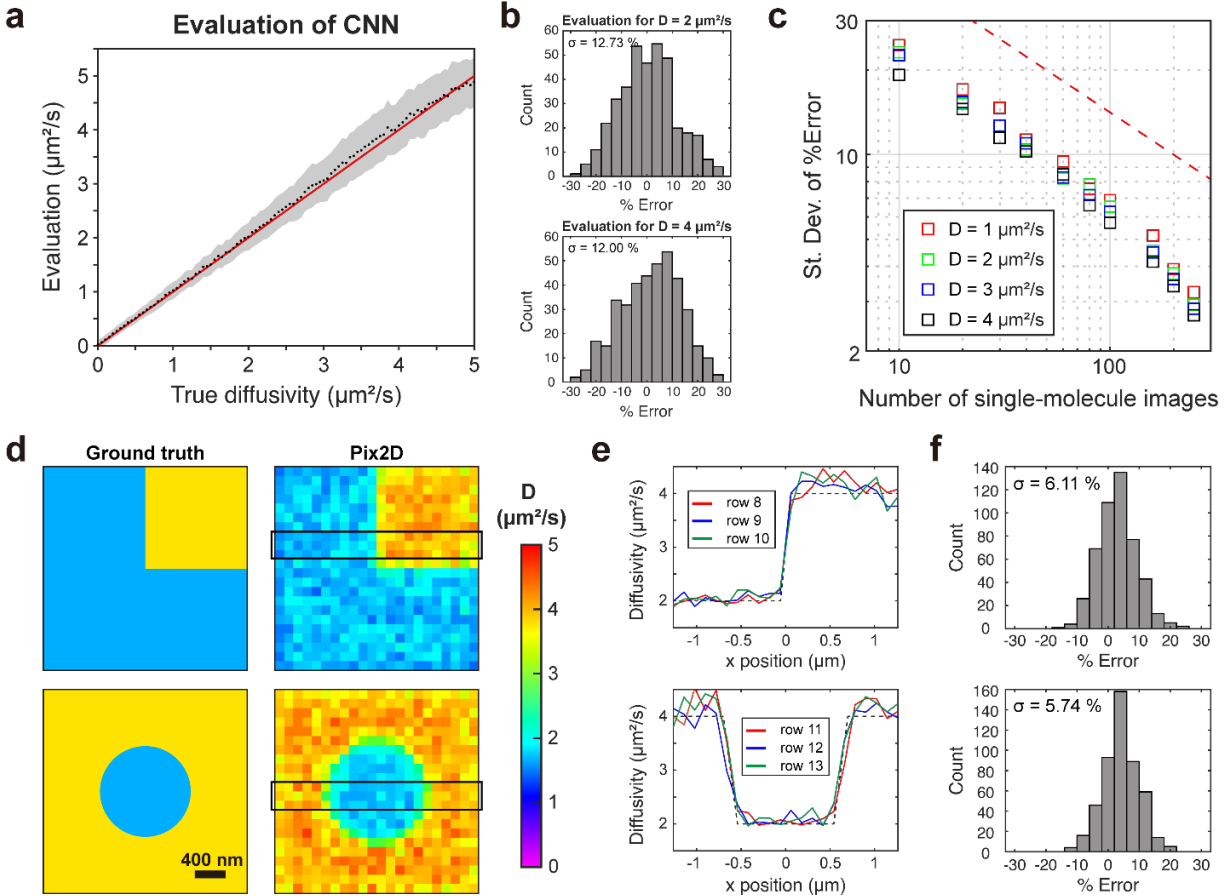
Figure 12. Performance assessment for Pix2D CNN.

(a) Validation of the trained CNN using simulated data not included in the training, for input channel size n_{ch} = 40. For each D value, evaluations were performed for 400 sets of n_{ch} images, and the average value and standard deviation were plotted as a black marker and the shaded area, respectively. Red line: reference (evaluation equaling the ground truth). (b) Distributions of relative errors (%Error) for training labels of D = 2 and 4 μm²/s. (c) Standard deviations of %Error for D = 1, 2, 3, and 4 μm²/s for different counts of starting single-molecule images (p^i), but fixed n_{ch} = 40. Red dashed line: trend based on MLE analysis of the distribution of single-molecule step distances. (d) Spatial mapping of simulated data. (Left) Ground truths of simulated patterns with spatially varied D values. (Right) Pix2D mapping results at a binning grid size of 120 nm, so that each bin counted ~200 simulated single-molecule images. (e) Line profiles in three rows of the Pix2D mapping results along the black boxes in (d). Dashed line: reference line of ground truth diffusivity. (f) Distribution of the %Error of Pix2D results in the different spatial bins, for all bins in (d).

that with maximum likelihood estimation (MLE) based on the distribution of step distances, the relative standard error in D equals to the inverse square root of the count of step distances.[45] For the same number of single-molecule images, the Pix2D standard errors were consistently ~2-fold lower (Figure 12c). This behavior is reasonable, considering that in Pix2D, each single-molecule image directly encodes motion in two dimensions, whereas for approaches based on the analysis of step distances, each step needs two single-molecule images, and each connected single-step displacement is along one direction.
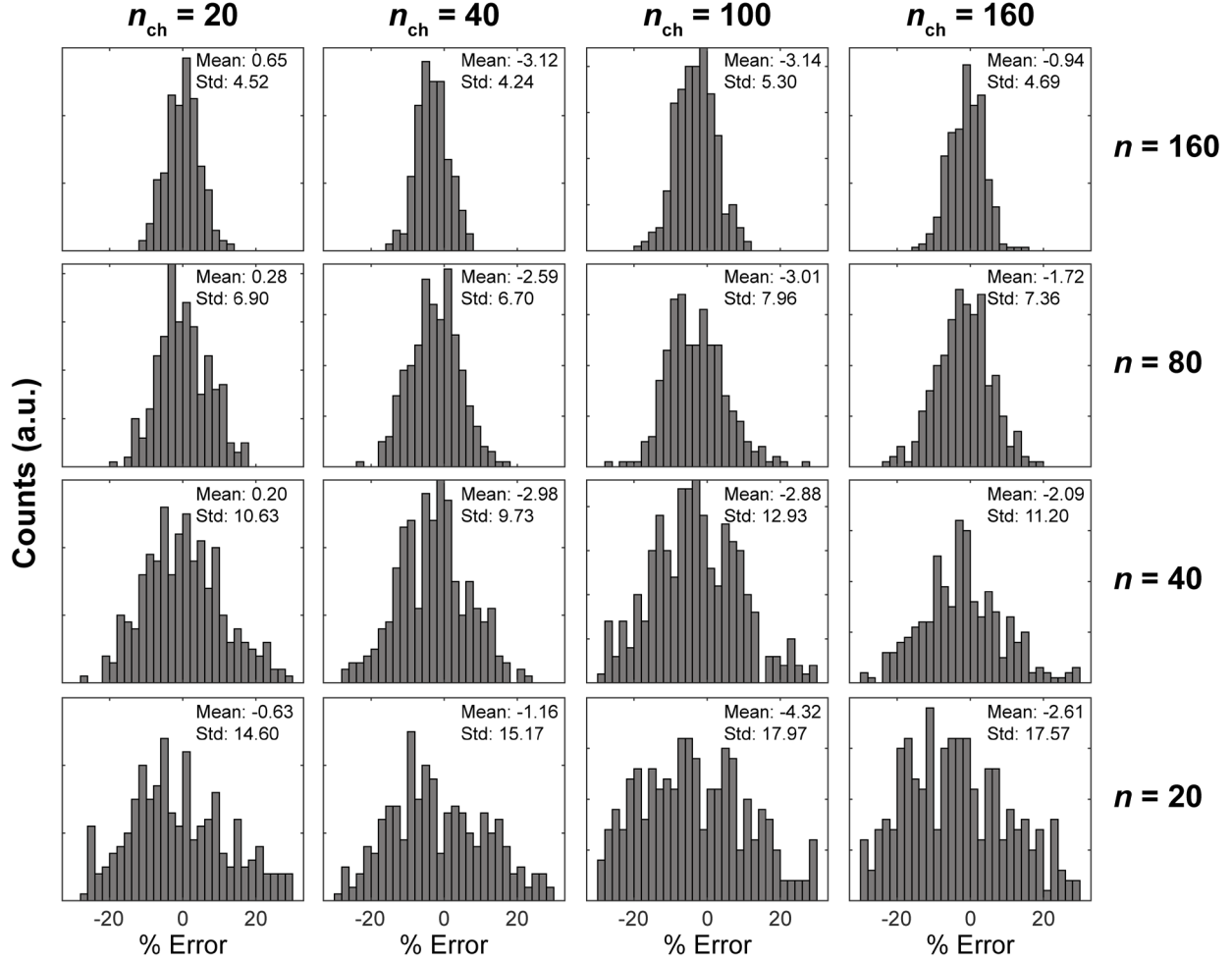
Figure 13. Performance assessment with different input channel sizes.
n (equivalent to p^i in each spatial bin when mapping) = 20, 40, 80, and 160 simulated single-molecule images of $D = 2$ µm²/s were processed with Pix2D of different input channel sizes n_{ch} = 20, 40, 100, and 160. For each dataset, $m = 100$ sets of n_{ch} sampling from n images were separately fed into the model as inputs, and the averaged output of the m sets was taken as the estimated D value. This process was repeated 300 times for each condition by randomly sampling n images, and the resultant 300 estimated D values were shown as histograms of % error from 2 µm²/s. a.u., arbitrary unit.

3.2.3. Spatial diffusivity mapping of simulated data.

To examine the performances of Pix2D for diffusivity mapping, we simulated spatial patterns, *e.g.*, square and circular shapes ~1 µm in size with contrasting regional D values of 2 and 4 µm²/s (Figure 12d, left). Single-molecule trajectories were simulated by randomly selecting the starting positions of the molecules and then updating D at every micro-step based on their new positions. The simulated single molecules were localized and spatially binned into a 120 nm × 120

nm grid, so that the resultant counts of molecules were ~200 per bin, comparable to the typical experimental super-resolution imaging data. Single-molecule images in each bin were then processed and fed into the model described above for diffusivity mapping (Figure 12d, right). We thus showed that our approach correctly mapped out spatial differences in diffusivity. Line profiles crossing the diffusion pattern boundaries showed sharp transitions in the mapped D values (Figure 12e), so that full transitions were accomplished within ~2 bins (~240 nm). Relative errors to the ground truths were <10% for most bins for the entire images (Figure 12f).

3.2.4. D mapping of experimental data on supported lipid bilayers.

To apply the above model trained with simulated datasets to experimental single-molecule images, we first augmented the training data to deal with two potentially highly variable parameters, the brightness of molecules and background noise. We adapted domain randomization[97] to achieve performance invariant toward these two parameters. Multiple training datasets were generated from combinations of different photon counts and background noise levels when mapping the diffusion trajectories to images. The ranges of these parameters were set to mimic the typical distributions of single-molecule brightness and background of wide-field single-molecule images. The resultant model performed robustly for different combinations of parameters both not covered (Figure 14) and covered (Figure 15) in the augmentation.

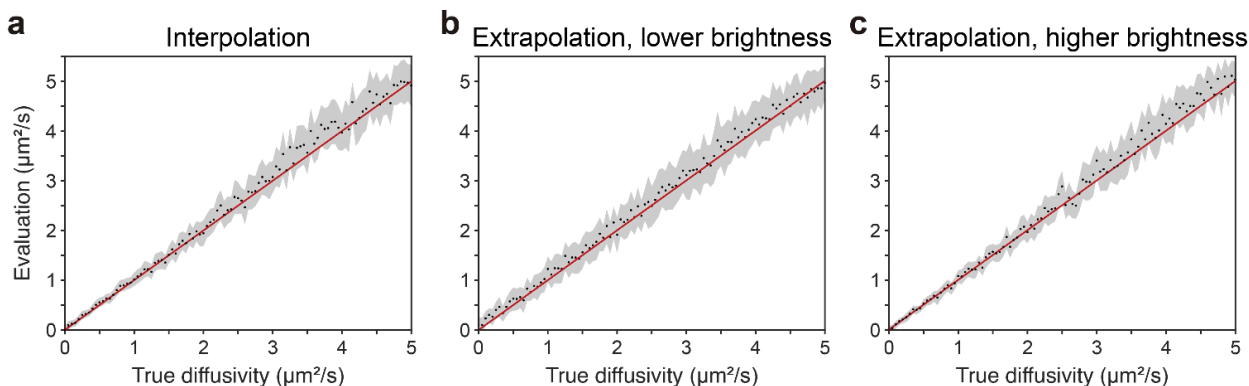**Figure 14. Interpolation and extrapolation performances of the trained model.**
Evaluation of the model with simulated datasets with background noise and brightness levels not used for the training, including (a) interpolation with values between the training noise and brightness levels and (b) extrapolation with lower (360 photons) and (c) higher (1350 photons) brightness levels outside the training range.

24
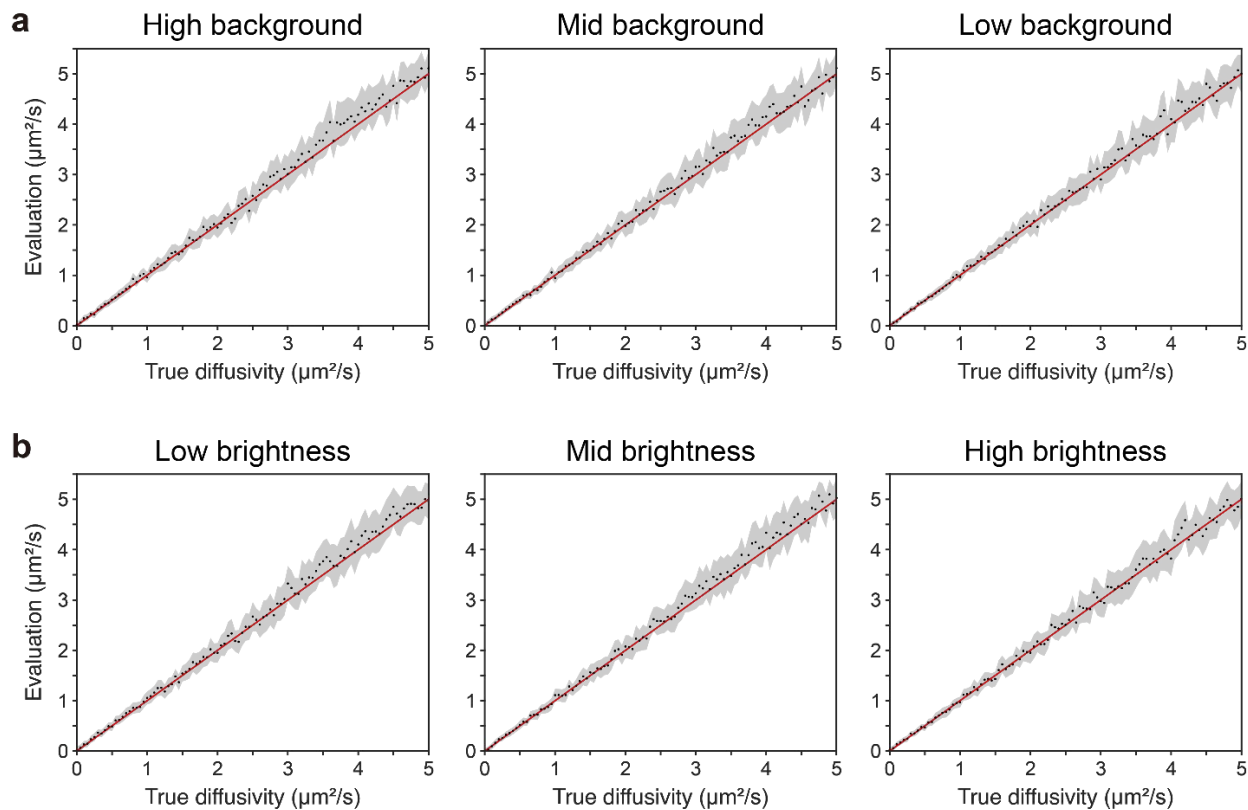
Figure 15. Evaluation of the data augmentation method for the model training.

The model was trained with the data augmentation method of diversifying background noise levels and single-molecule brightness levels. (a) Validations of the model for different simulated background noise levels typical to our experiment data, with input channel size n_{ch} = 40. For each D value, evaluations were performed for 100 sets of n_{ch} images, and the average value and standard deviation were plotted as a black marker and the shaded area, respectively. Red line: reference (evaluation equaling the ground truth). (b) Validations of the model for different simulated single-molecule brightness levels typical to our experimental data.

Experimental single-molecule images were obtained with a typical SMLM setup for BDP-TMR-alkyne, which reversibly intercalated into supported lipid bilayers (SLBs) to report the lateral diffusivity of the membrane.[44] Single-molecule images (Figure 16a) were collected with an exposure time of 9 ms per frame under typical SMLM conditions for SLBs prepared from pure 1,2-dioleoyl-*sn*-glycero-3-phosphocholine (DOPC) and mixtures of DOPC:bSM (brain sphingomyelin) 1:1 (mol%) and DOPC:bSM:cholesterol 1:1:1 (mol%). The localized single-molecule images were processed through Pix2D to generate diffusivity maps. Each spatially homogeneous, yet separately distinct diffusion coefficients were thus visualized for the three SLBs (Figure 16b). Statistics of the evaluation results of different spatial bins yielded D = 3.21±0.45, 2.48±0.46, and 1.09±0.28 μm^2/s, respectively, for the three SLBs (Figure 16c). These values are comparable to previously reported results, in which D ~3-4, ~2-3, and ~1 μm^2/s are reported for similar DOPC, DOPC:bSM, and DOPC:bSM:cholesterol SLBs at room temperature.[98,99] We also

performed single-particle tracking[68] on the data, but found most molecules only stayed in the SLB for a few frames (Figure 17), as is typical in PAINT-type SMLM.[8] Mean squared displacement (MSD) analysis on the occasionally observed long traces (Figure 18) yielded the same trends for the three SLBs, consistent with the notion that diffusion is slower in the more densely packed phases containing saturated lipids and cholesterol.[98,99]
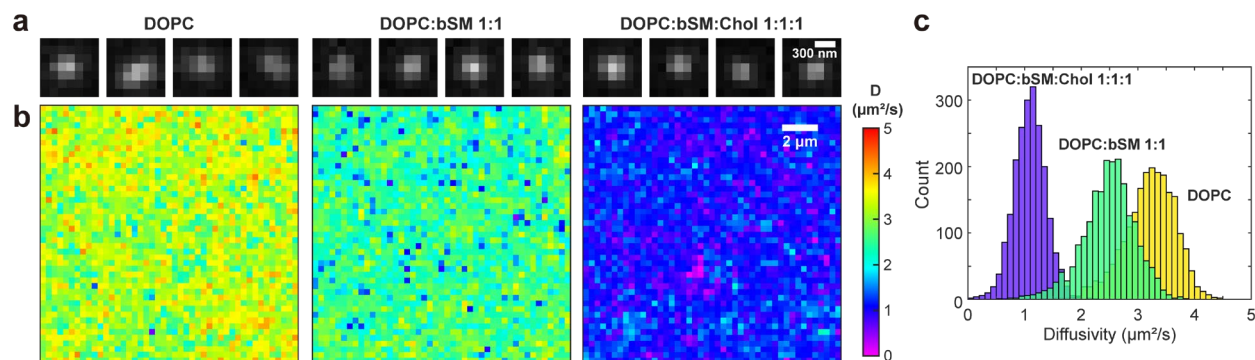
Figure 16. Pix2D applied to experimental data on single molecules diffusing in SLBs.

(a) Example wide-field single-molecule images collected at an exposure time of 9 ms per frame, for BDP-TMR-alkyne diffusing in SLBs of different compositions: DOPC only, DOPC:bSM 1:1 (mol%), and DOPC:bSM:cholesterol 1:1:1 (mol%). (b) Color-coded D maps of the three samples generated by spatially binning the single-molecule images accumulated over 30,000 frames onto a 320 nm × 320 nm grid, and then feeding the resultant ~200 single-molecule images in each bin into the Pix2D CNN for evaluation of local D. (c) Distributions of the evaluated D values in each bin for the three samples, corresponding to 3.21±0.45, 2.48±0.46, and 1.09±0.28 μm^2/s, respectively.
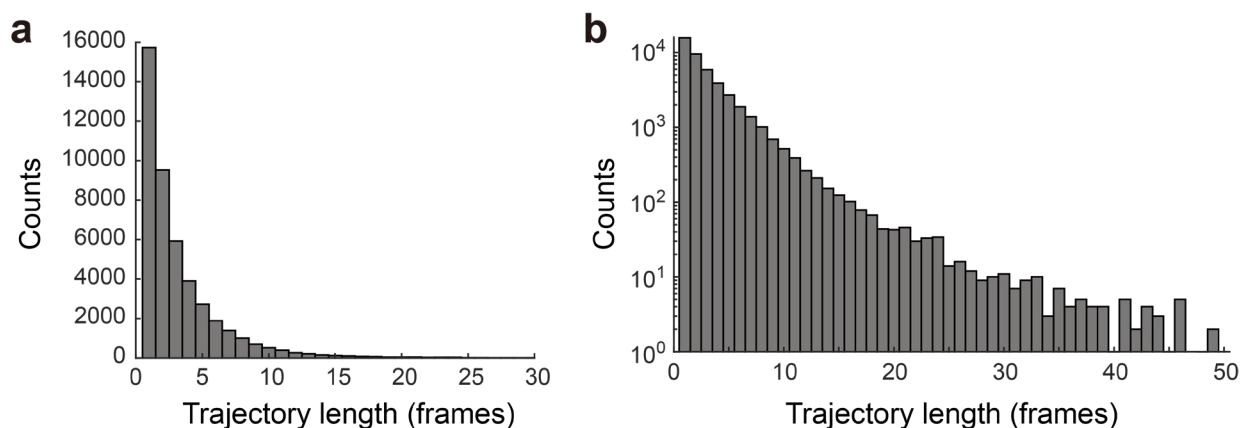
Figure 17. SLB dwell time of BDP-TMR-alkyne single molecules.

Plotted: Distribution of trajectory lengths in a typical experiment for BDP-TMR-alkyne single molecules diffusing in a DOPC SLB, plotted on the linear (a) and logarithmic (b) scales for the counts, respectively. Data was collected at a framerate of 110 frames per second. Tracking was performed using TrackMate[100].
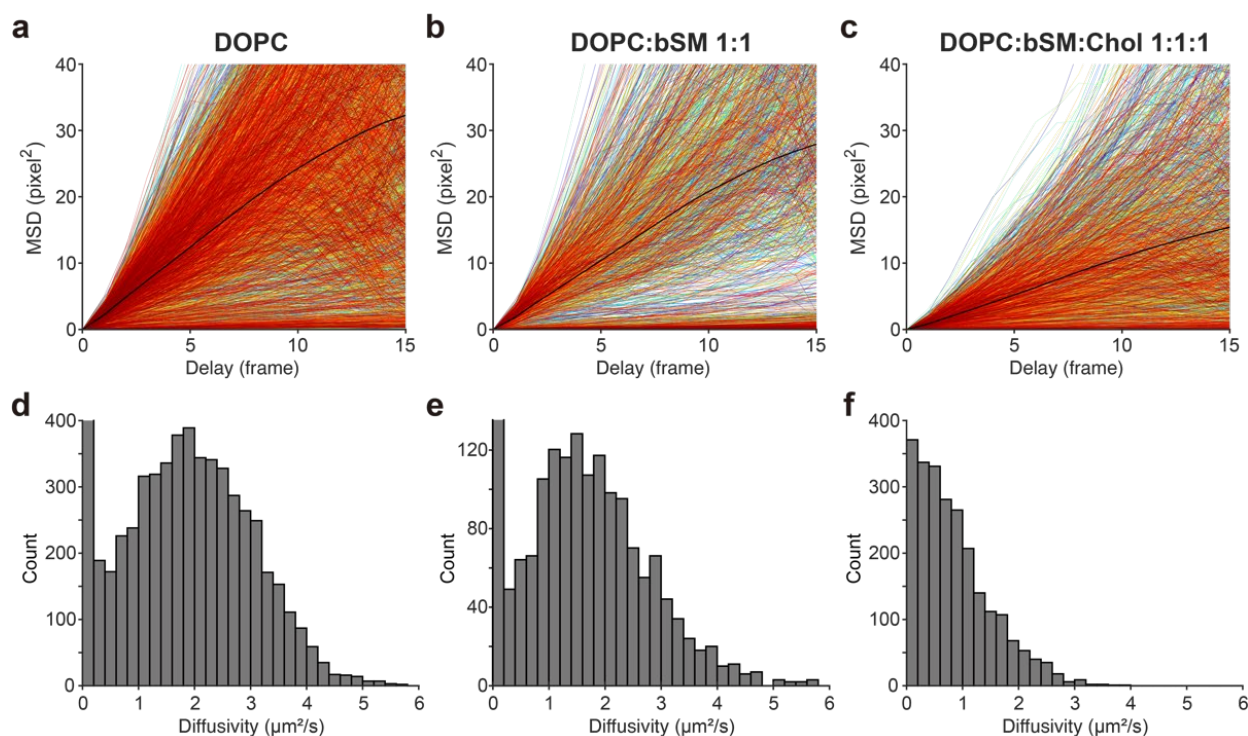
Figure 18. MSD analysis of BDP-TMR-alkyne single molecules diffusing in different SLBs.

MSD analysis was performed using MSDanalyzer[101] for BDP-TMR-alkyne single molecules in the data of Figure 3 for three SLBs compositions: DOPC, DOPC:bSM 1:1, and DOPC:bSM:Chol 1:1:1. Images were acquired at 110 frames per second with a pixel size of 160 nm. Trajectories 15-40 frames in length were selected for the MSD analysis, and the first 25% of MSD curves were used for fitting *D*. *e.g.*, A delay range of 1 to 5 frames was used for a trajectory length of 21. (a-c) MSD curves and weighted-average MSD curves (black) for trajectories in the DOPC (a), DOPC:bSM 1:1 (b), and DOPC:bSM:Chol 1:1:1 (c) SLBs, respectively. (d-f) Distribution of fitted single-molecule *D* values from the MSD curves. Consistent decreasing trends in *D* were observed for the 3 SLBs, even though the distributions were board due to the limited trajectory lengths, and the absolute values generally appeared lower, possibly owing to statistical biases in which the slower-diffusing molecules had higher chances to stay longer in the SLBs to yield the rare long tracks.

3.2.5. *D* mapping of microdomains in supported lipid bilayers.

To further assess mapping capabilities, we prepared SLBs with spatially separated domains. With a 60:40 mixture of DOPC and 1,2-dipalmitoyl-*sn*-glycero-3-phosphocholine (DPPC), we generated SLBs in which DOPC and DPPC respectively segregated into the fluid and gel phases at room temperature.[102] SMLM super-resolution images (Figure 20a) of BDP-TMR-alkyne single molecules collected at an exposure time of 9 ms per frame showed contrasting localization densities for the DOPC and DPPC domains, as the higher packing order of aliphatic chains of the gel phase DPPC limited fluorophore access.[103] This difference in localization density

disappeared upon melting of the DPPC domains at high temperatures (Figure 19). Binning the accumulated single-molecule images with a 120 nm × 120 nm grid allowed mapping of local D with Pix2D (Figure 20b). Contrasting D was thus unveiled for the two lipid phases. Temporally dividing the collected single-molecule data into two periods of 3.4-min durations for their separate Pix2D evaluations further yielded D maps comparable to the entire dataset (Figure 21), thus demonstrating that the diffusivity spatial patterns remained unchanged over the recording time.
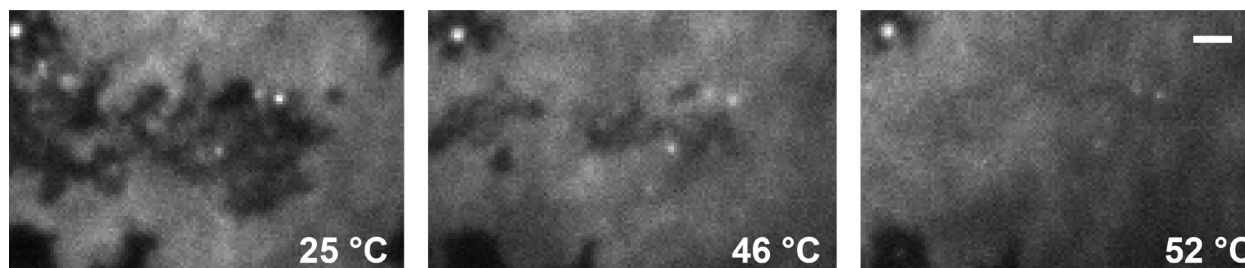
Figure 19. Melting of DPPC domains.
Real-time epifluorescence images of a 60:40 DOPC:DPPC SLB stained with BDP-TMR-alkyne. At room temperature, DPPC domains appeared darker due to limited access for BDP-TMR-alkyne (left). Melting of DPPC domains at elevated temperatures allowed the mixing of DPPC and DOPC domains and BDP-TMR-alkyne intercalation, and so the contrast differences diminished (middle and right). Scale bar: 2 µm.
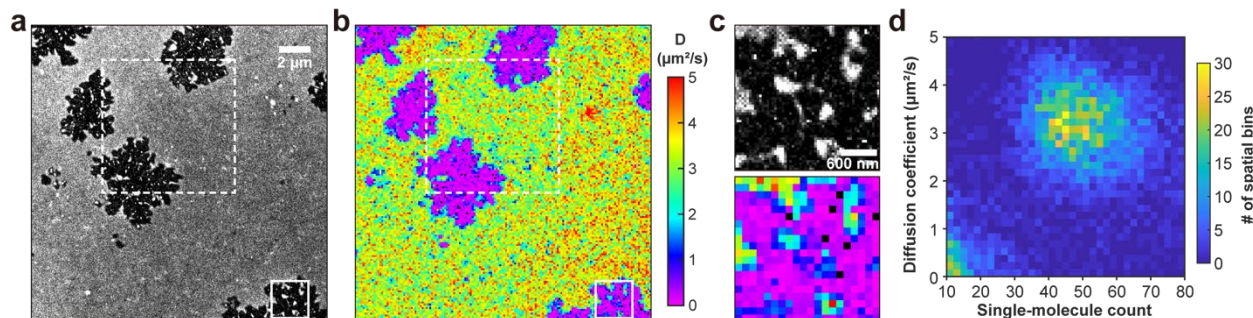
Figure 20. Pix2D D mapping of SLB microdomains.
(a) SMLM super-resolution image of an SLB of 60:40 DOPC:DPPC, presented as the local counts of single BDP-TMR-alkyne molecules recorded over 45,000 frames at 110 frames per second with an exposure time of 9 ms per frame. (b) Color-coded D map generated by spatially binning the single-molecule images onto a 120 nm × 120 nm grid for the Pix2D evaluation of local D. (c) Zoom-in of the solid box-marked region in (a,b). (d) Two-dimensional distribution of the Pix2D-evaluated D versus single-molecule count for the different spatial bins in the dashed box-marked region in (a,b).

Comparison of the Pix2D D map (Figure 20b) with the SMLM image (Figure 20a) showed good correlations: The high-count regions (DOPC phase) consistently exhibited high D of ~3.2 µm²/s, close to our above results on the single-component DOPC SLB (Figure 16). Meanwhile, the low-count regions (DPPC phase) exhibited $D < $~0.5 µm²/s, consistent with the notion that this gel phase is nonfluidic at room temperature. Notably, features down to ~300 nm were well-resolved in the Pix2D D map (Figure 20c), in agreement with our simulation results (Figure 20d,e).

Distribution of the evaluated local D values in each spatial bin versus the count of molecules in the bin further showed a good correlation that fast diffusion was exclusively observed for the high-count DOPC phase (Figure 20d).
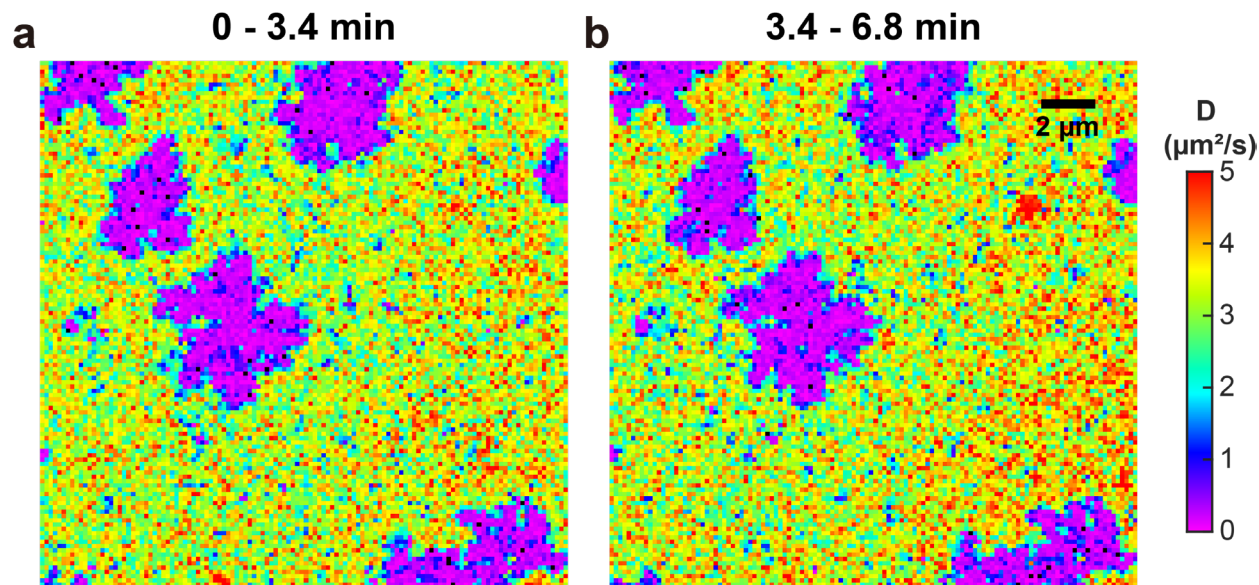
Figure 21. Time-resolved Pix2D results.

The original single-molecule data of Figure 20b collected over 6.8 min was divided into two periods of 3.4-min duration each. The two divided datasets were separately fed into Pix2D to generate two independent diffusivity maps at a 160 nm × 160 nm spatial bin size. D maps comparable to Figure 20b were obtained for both periods, thus demonstrating that the diffusion spatial patterns remained unchanged over the recording time, as well as that viable D maps can be obtained at ~3 min time resolution.

3.3. Conclusion

While critical to biological processes, molecular diffusion has been difficult to quantify, and spatial mapping of local diffusivity is even more challenging. In this work, we exploited the often undesired yet evident motion blur of single-molecule images, recorded under typical SMLM conditions, to extract diffusion coefficient D and further enable spatial mapping. Many recent efforts have successfully applied machine learning to single-molecule images in SMLM contexts to assist three-dimensional localization and color separation, as well as to extract optical parameters such as the Zernike coefficients and fluorescent backgrounds[73–85] In this study, we instead focused on extracting higher-dimensional, functional information[104] on molecular diffusion from the single-molecule images.

Different from previous machine-learning studies in which the parameters in question are directly projected to single-molecule images with a fixed pattern, the stochastic nature of diffusion mandates that even for a fixed D value, the diffusion trajectory of a molecule in a fixed time window (and thus motion blur) takes diverse forms not unique to the given D. Thus, rather than

attempting to assign a D value to each single-molecule image, we constructed a model that took a stack (n_{ch}~40 channels) of uncorrelated single-molecule images as the input and evaluated a D value as the output. For input data of different numbers of single-molecule images, m~100 sets of n_{ch} samplings were separately fed into the model, and the averaged output of the m datasets was taken as the final D value. This model architecture of fixed channel numbers simplified implementation, while the m-time sampling provided flexibility for the number of source single-molecule images. These advantages proved instrumental to spatial mapping: we thus were able to spatially grid all the collected single-molecule images and separately fed the images in each spatial bin to the CNN model to evaluate local D, without having to worry about the different counts of molecules in each bin.

With simulated data of known ground truths, we thus showed that our above Pix2D approach correctly extracted D from single-molecule image stacks. With 40 source single-molecule images, the typical relative standard error σ_{error} was ~12% over a wide D range, and the evaluation results were robust towards different brightness and background noise levels. This evaluation error was ~2-fold better than that based on the MLE analysis of single-molecule step distances, and decreased monotonically for increased numbers of single-molecule images with little dependence on n_{ch}.

With experimental data on BDP-TMR-alkyne single molecules that dynamically entered SLBs and stayed for short durations, we next showed that Pix2D successfully resolved the different diffusivities for bilayers of different lipid compositions, with the resulting D value trends matching that expected based on previous bulk measurements. For the phase-separated DOPC-DPPC mixture system, we further demonstrated that Pix2D resolved the different D values in the two phases at the nanoscale.

Together, by directly linking stacks of uncorrelated single-molecule images to diffusivity, we have successfully extracted D values from both simulated and experimental data, and further achieved spatial mapping under SMLM settings. Whereas with phase-separated SLBs we have resolved spatial patterns in the environment, the capability of detecting local diffusivities may also be harnessed to report on changes in the states of the diffusers themselves, *e.g.*, oligomerizations and conformational changes. While in this work we have focused on the direct extraction of diffusivity from single-molecule images in individual frames, future efforts may consider connecting molecules spanning consecutive frames to further enhance prediction. The possible extension of the approaches developed in this work to diffusion in three dimensions, as well as to other high-dimensional single-molecule signal dimensions,[14] represent additional exciting challenges.

3.4. Materials and method

Data simulation

For training and test data, single-molecule images were generated from Monte Carlo two-dimensional Brownian diffusion simulation. For each molecule, a Brownian trajectory of 9 ms was simulated through 1,000 micro-steps of random two-dimensional motion of distance $\sqrt{4Dt}$ using the local diffusion coefficient D and the simulation interval t. The simulated trajectory was mapped onto the pixelized image grid using typical photon counts of 60-120 photons per ms and the microscope PSF profile experimentally determined using 100-nm fluorescence beads. Background noise was further added to each pixel based on the typical values observed with the recording camera.

Model architecture, training, and application

The Pix2D CNN model was designed to take a stack (n_{ch} channels) of single-molecule images, each cropped at 7×7 pixels, as the input, and predict a D value as the output. The architecture stacked multiple convolutional layers, a fully connected layer, and the final regression layer (Figure 10). The final prediction was computed by a fully connected layer, followed by a regression layer that calculated the mean square error (MSE) losses between the predicted values and the ground truth labels. Design methodologies of ResNet[93] were partially followed, so that the building blocks entailed a convolutional layer with a kernel size of 3, Swish activations,[95] and batch normalization layers.[94] As we performed regression for predicting continuous D values, we used Swish activation instead of the ReLU activation used in the original ResNet model. The training dataset was constructed for 121 labels of diffusion coefficients, from 0 to 6 μm^2/s in 0.05 μm^2/s intervals. For each diffusion coefficient label, 100 training inputs of $n_{ch} = 40$ simulated 7×7 pixels single-molecule images were used. Therefore, the training dataset had 12,100 inputs of the dimension of 7×7×40, for which we further augmented 20 combinations of single-molecule brightnesses and image backgrounds. Further increasing the training dataset size did not further improve the prediction accuracy. The training objective was the MSE loss between the predicted diffusivity and the target diffusivity using stochastic gradient descent (SGD) with momentum as the optimizer. Training was performed over 60 epochs with a batch size of 128, and an initial learning rate of 0.003. The learning rate was decreased by 10x after every 25 epochs. To apply the trained CNN model, $m = 100$ datasets, each with the same dimensionality as the training data – thus m different $7 \times 7 \times n_{ch}$ arrays – were generated by random sampling from the p^i input images for feeding into the model. For bins having $p^i < n_{ch}$, each input is generated by allowing repeated sampling of each image, yet limiting the repetition to the minimum integer j satisfying the following condition: $j \times p^i > n_{ch}$. The resultant m outputs from the model were averaged to yield the final diffusivity. Negative final values were treated as zero for physical relevance.

SLB preparation

Lipids (Avanti Polar Lipids 850375, 850355, and 860062) and cholesterol (Sigma, C8667) were dissolved in chloroform as 5 mg/mL stock solutions. The lipid mixture was combined in a 25-mL round bottom flask with the desired ratio from the stock solution. The solvent was removed under a stream of nitrogen gas. The resulting lipid film was rehydrated in 60 °C Milli-Q water and vortexed to a final concentration of 1 mg/mL multi-lamellar vesicle (MLV) solution. The MLV solution was then extruded at 60 °C over 11 times through a 100 nm polycarbonate membrane filter (Avanti Mini Extruder) to form small unilamellar vesicles (SUVs). The SUV solution was diluted in a 2:1:1 mixture of PBS (phosphate-buffered saline):H_2O:SUV and sonicated until deposited on a piranha-etched coverslip. Excess, unruptured vesicles were removed after 20 minutes by washing with PBS. 1 nM of BDP-TMR-alkyne (A24B0, Lumiprobe) in PBS was used for the single-molecule imaging of SLBs.

Single-molecule imaging

Fluorescence imaging was performed on a Nikon Ti-E inverted fluorescence microscope. A 561 nm laser (OBIS 561 LS, Coherent, 165 mW) was focused at the back focal plane of an oil-immersion objective lens (Nikon CFI Plan Apochromat λ 100×, numerical aperture 1.45) to continuously illuminate the sample at ~1 kW/cm^2. A translation stage shifted the laser beams toward the edge of the objective lens, so the light reached the sample at an incidence angle close to the critical angle of the glass-water interface to achieve a near-total internal reflection condition. Wide-field single-molecule images were filtered by a long-pass filter (ET575lp, Chroma) and a band-pass filter (ET605/70m, Chroma), and recorded continuously using an EM-CCD camera (iXon Ultra 897, Andor) in the frame-transfer mode at 110 frames per second (fps) with a frame integration time of 9 ms. The typically recorded photon counts were 500-1200 for each BDP-TMR-alkyne molecule. 30,000-50,000 frames were typically recorded for each sample.

Processing of single-molecule images

Single molecules were first identified and localized with established methods using Insight3 (Dr. Bo Huang at University of California, San Francisco, and Dr. Xiaowei Zhuang at Harvard University), yielding typical densities of ~0.1 molecules/μm^2/frame. An ROI of 7×7 pixels was sampled around the center of each localized molecule, and molecules with overlapping ROIs were discarded. The single-molecule images were then spatially binned with a fixed grid size (*e.g.*, 120 nm × 120 nm). For bins having single-molecule count $p^i > 10$, the accumulated single-molecule images were fed into the trained Pix2D model as described above for the evaluation of local D.

Chapter 4: Conclusion and outlooks

Optical microscopy has been one of the most widespread and important tools for biophysical studies by allowing researchers to observe biological processes at high spatial and temporal resolution. Advances and engineering in this tool, such as super-resolution microscopy[6–8] and fluorescence correlation spectroscopy (FCS),[59,61–64] have further extended the application of optical microscopy by breaking the spatial resolution limit and providing additional information beyond spatial coordinates, respectively. Nonetheless, microscopic techniques are being revolutionized toward analyzing the physical properties of the sample and the correlation to the structural information.[14–16] In particular, single-molecule and protein diffusion studies have provided unprecedented insights into the molecular mechanisms of biological systems as many fundamental processes are carried out by the Brownian motions of molecules.[20–24,58–60] Such understanding of the system is also crucial for a wide range of biomedical applications, including drug delivery, tissue engineering, and diagnostics.[30–33]

In recent years, our research group has introduced single-molecule displacement/diffusivity mapping (SMdM), which can trace single molecules with high fidelity and high throughput as fast as hundreds of μm^2/s, that corresponds to the diffusivity of smaller molecules of size around 1 kDa. In Chapter 2, I presented the application of SMdM for studying the suppression of molecular diffusion in hydrogel nanomatrices with a controlled meshwork size. By repurposing expansion microscopy and modulating a range of polymer fractions, we showed that larger molecules experience greater suppression of diffusion under the fixed meshwork size and that, as the meshwork size was reduced, diffusion was progressively suppressed, with this effect being more pronounced for larger molecules. The obstruction by the meshwork was found to be independent of the suppression of diffusion from increased solution viscosity. These two mechanisms work separately to reduce molecular diffusivity and produce the final diffusion slowdown in complex systems such as cells. The study's findings have potential implications for the development of manipulation and measurement tools using expandable hydrogels and expansion microscopy.

In the following chapter, I demonstrated the high-resolution diffusivity mapping with deep learning that can correlate to the super-resolution imaging from typical single-molecule localization microscopy settings. We took advantage of the motion blur of the single molecules recorded in the camera frame to extract how fast the molecules move, thus diffusion coefficient D, without fitting the single-molecule images into any physical models. With both simulated and experimental data, the trained model correctly extracted diffusion coefficients and successfully resolved spatial patterns that were coherent to the sample structures at nanoscale. Future efforts may consider extending the approaches developed in this work to diffusion in three dimensions and correlative analysis with additional physical properties from single-molecule signals.

The following section describes another example of SM*d*M application, that high statistical reliability of the method in measuring the diffusivity of different enzymes under their enzymatic activities. Unlike some recent studies that suggested those reactions accelerate the diffusion of these proteins, our results disprove the hypothesis as all enzymes measured with SM*d*M showed no significant difference whether or not they are in enzymatic reaction. Additionally, I present the validation of multiple-component model analysis of SM*d*M data using simulated dataset and experimental results.

4.1. Application of SM*d*M: Disproval of enzymatic diffusion enhancement

The work in this part was conducted in collaboration with Alexander A. Choi, Kun Chen, Rui Yan, Wan Li and Ke Xu. It is reproduced in part here from ref.[45] and with permission from all coauthors. Copyright 2022 American Chemical Society.

Here, I present the application of SM*d*M taking advantage of its high-throughput nature, experimental results disproving the hypothesis that catalytic reaction can increase the D of enzymes. We aimed to measure the D of four enzymes during catalytic turnovers by analyzing the statistics of transient displacements of single molecules in common buffers. The precise measurements of D showed that there were no changes in the diffusivity of catalase, urease, aldolase, and alkaline phosphatase, over a wide range of substrate concentrations. Our study employing a single-molecule approach that overcame limitations and artifacts observed in previous studies thus indicates that enzymatic reactions do not enhance diffusion.

4.1.1. Controversy and debates on enzymatic diffusion enhancement from its reaction

The recent reporting of accelerated diffusion of enzymes in catalytic reactions has generated keen research interest and debate.[105–112] Measurements based on fluorescence correlation spectroscopy (FCS) have documented substantial (>~30%) increases in the diffusion coefficient D for multiple enzymes under catalytic turnovers.[105,106,113–120] Several recent studies, however, emphasize FCS artifacts[107,121,122] and report contradicting results. Dynamic light scattering (DLS) experiments, with low sensitivity for the very small sizes of proteins, also yield inconsistent results either supporting[118,120] or refuting[123] substrate-enhanced diffusion. Likewise, different nuclear magnetic resonance (NMR) experiments have separately reported the presence or absence of reaction-enhanced D for enzymes and small molecules,[124–127] with unsettled debate on data interpretation.[112,128,129]

Single-molecule experiments[22,130,131] provide potential means to achieve precise D measurements by probing one molecule at a time. However, with expected $D\sim$30-50 $\mu m^2/s$,[50,110] the fast motions of typical enzymes make it difficult to detect freely diffusing single molecules. Using reducing-oxidizing chemicals that suppress fluorophore blinking, a recent study achieved long-time anti-Brownian electrokinetic (ABEL) single-molecule trapping of dye-labeled alkaline phosphatase (ALP) to show no change in D with the addition of its substrate.[122] Meanwhile, single-molecule tracking has been reported for dye-labeled urease and ALP that were substantially slowed down by using viscous reagents as methylcellulose[132,133] and glycerol[122,133] or by tethering to supported lipid bilayers,[133] which yielded contrasting results of no change versus up to 3-fold increases in D upon substrate addition. Thus, it remains difficult to quantify D through single-molecule measurements for molecules freely diffusing in regular buffers, whereas the addition of blinking-suppressing chemicals and viscous reagents complicates data interpretation.

4.1.2. Validation of SMdM statistical reliability

To obtain statistical validity and robustness for diffusivity of enzymes, $>5\times10^4$ single-molecule displacements were typically accumulated for SMdM analysis. Under such conditions, maximum likelihood estimation (MLE) with a predefined model based on normal diffusion plus background yielded good fits, from which D values were obtained with their 95% confidence intervals, *e.g.*, $D = 47.3\pm0.4$ $\mu m^2/s$ for Cy3B-labeled catalase in phosphate-buffered saline (PBS) (Figure 22a). We employed SMdM to measure the diffusion coefficients of 13 different protein samples in a wide 14-545 kDa size range in PBS and Tris buffers (Figure 22b) and obtained results in agreement with that is predicted by the Young-Carroad-Bell model,[50,110] including for the fast-diffusing small proteins as RNase A and lysozyme at >100 $\mu m^2/s$.

To define how the achievable precision in D depends on the count of single-molecule displacements N, we simulated 600-μs displacements d for molecules diffusing at $D = 50$ $\mu m^2/s$. Different levels of backgrounds were further included, *i.e.*, assuming 0%, 10%, or 25% of the total counts were due to extraneous molecules that randomly entered the vicinity during Δt. MLE of the simulated data showed that with zero background, the relative uncertainty of D (σ_D/D) was $\sim 1/\sqrt{N}$, so that 10% and 1% uncertainties were achieved with 100 and 10,000 counts of d, respectively (Figure 22c). This result is expected: each displacement provides an independent reporting of diffusivity, so the signal-to-noise ratio improves as $\sim\sqrt{N}$. At background levels of 10% and 25%, 1% uncertainty in D was achieved with $\sim$20,000 and $\sim$30,000 counts of d, respectively. As our experimental data contained $<$10% background, $\sim$0.5% relative uncertainty (hence an $\sim\pm$1% bracket for the 95% confidence interval) was thus obtained (Figure 22c) with the typical $>$50,000 counts of d in our experiments, in agreement with our above MLE results on the experimental data (Figure 22a).
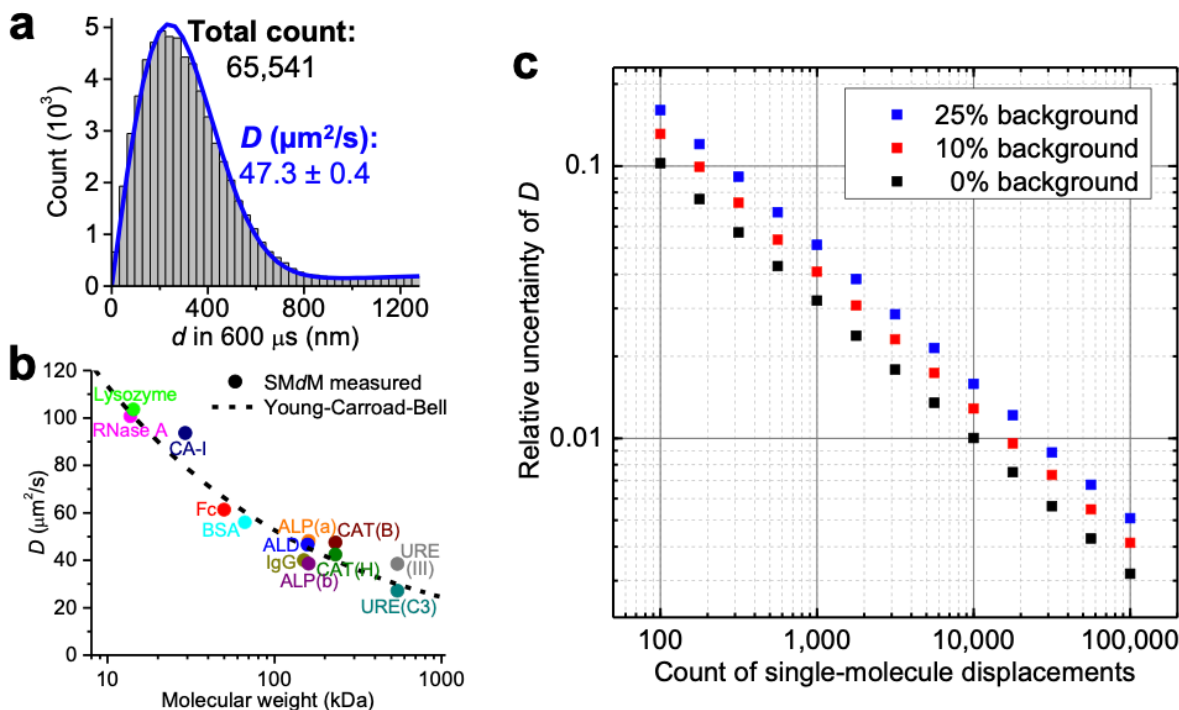
Figure 22. High-throughput statistics of single-molecule displacements for precise diffusivity analysis. (a) Histogram: distribution of the 65,541 transient single-molecule displacements collected in 9 min by repeating the tandem excitation scheme 30,000 times. Blue line: MLE yielding a diffusion coefficient D of 47.3 ± 0.4 $\mu m^2/s$ (95% confidence interval). (b) SMdM-measured D values of 13 different protein samples of varying sizes in PBS and Tris buffers. Dash line: expected values at 20 °C according to the Young-Carroad-Bell model. (c) Relative uncertainty of D (σ_D/D) from MLE results of the simulated data at different levels of backgrounds, as a function of the counts of displacements. The standard deviations σ_D were calculated from the differences between 5,000 rounds of simulations under each condition.

4.1.3. SMdM measurements of enzymes under their catalytic activities

For catalytic reactions, we started with catalase in the presence of its substrate H_2O_2, for which system FCS has reported ~30-40% increase in D with ~25 mM H_2O_2.[106,113,115] SMdM statistics showed that the addition of 1, 5, and 50 mM H_2O_2 did not noticeably shift the single-molecule displacement distribution (Figure 23a). The catalytic reaction generated oxygen bubbles, which were more notable for samples with higher H_2O_2 concentrations (Figure 23a inset). The bubbles scattered light and increased the fluorescence background to slightly reduce our capability to track molecules across the tandem frames, and so led to a moderately increased tail in the d distribution (Figure 23a). Nonetheless, MLE yielded good fits (Figure 23b), and the resultant D values showed minimal variations in the range of 46.5-48.0 $\mu m^2/s$ between the different substrate concentrations (Figure 23c). These results contrast with the ~30-40% substrate-induced D enhancements reported in previous FCS studies.[106,113,115]

We next examined urease, for which previous FCS experiments have reported up to ~40% D enhancement in the presence of 10-100 mM of its substrate urea.[105,106,116,118–120] Moreover, ~3-fold substrate-induced D enhancement is recently reported for single urease molecules diffusing in the highly crowded or membrane-tethered systems at orders of magnitudes lower D values.[132,133] SMdM showed virtually identical distributions for the 600-µs single-molecule displacements of urease in PBS with and without the addition of 0.1-100 mM of urea (Figure 24a). MLE hence yielded comparable D values of 26.4-27.3 µm²/s for the five conditions with no noticeable trend on the substrate concentration (Figure 24b).
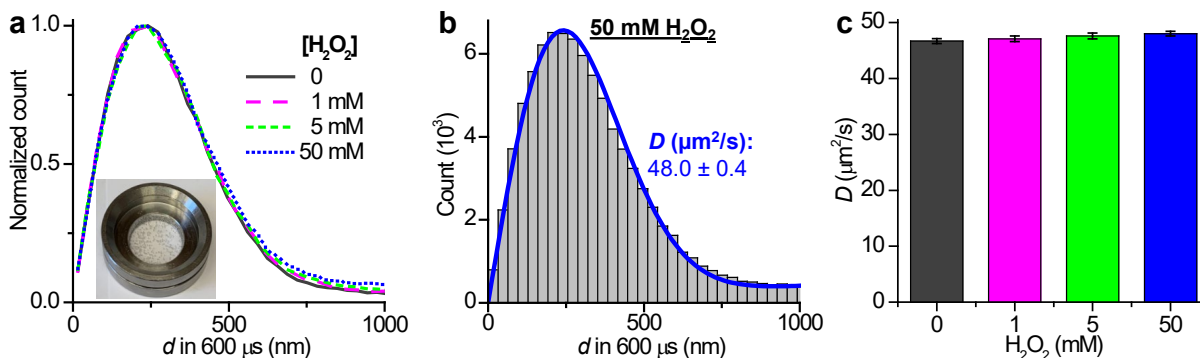

Figure 23. No substantial change in single-molecule displacements for catalase under turnover.
(a) Normalized count distributions of the measured 600-µs single-molecule displacements for Cy3B-labeled catalase diffusing in PBS buffers with H_2O_2 added at 0, 1, 5, and 50 mM. Inset: photo of a sample with 50 mM H_2O_2, showing the generation of bubbles from the catalytic reaction. (b) Histogram: the count distribution with the 50 mM H_2O_2 solution. Blue line: MLE yielding $D = 48.0\pm0.4$ µm²/s (95% confidence interval). (c) MLE-determined D at the different substrate concentrations. Error bars: 95% confidence intervals of MLE.

For ALP, FCS has initially reported up to an 80% increase in D with the addition of 2.6 mM of its substrate p-nitrophenyl phosphate (pNPP).[106] However, recent FCS experiments,[107,120,122] as well as single-molecule trapping in blinking-suppressed buffers and tracking in glycerol-slowed solutions[122] indicate no substrate-induced D enhancement. For ALP in its working buffer of 100 mM Tris-HCl (pH = 9.8) containing 1 mM $MgCl_2$ and 20 µM $ZnCl_2$, SMdM showed no substantial changes in single-molecule displacements with the addition of 0.5-10 mM pNPP (Figure 24c). Accordingly, the resultant D values of 46.8-48.1 µm²/s indicated no enhanced diffusion (Figure 24d).

We further examined aldolase, for which previous FCS experiments have either reported ~30% increase[114] or no change[118,120] of D in the presence of ~1 mM of its substrate, fructose 1,6-bisphosphate (FBP), whereas DLS[118,123] and NMR[125] experiments have indicated no D enhancement over broad substrate ranges. SMdM of aldolase in a HEPES buffer (pH = 7.4) showed no substantial changes in single-molecule displacements with and without the addition of 0.1-10 mM of FBP (Figure 24e), and hence no enhanced diffusion of D values in the range of 42.9-44.4 µm²/s (Figure 24f).
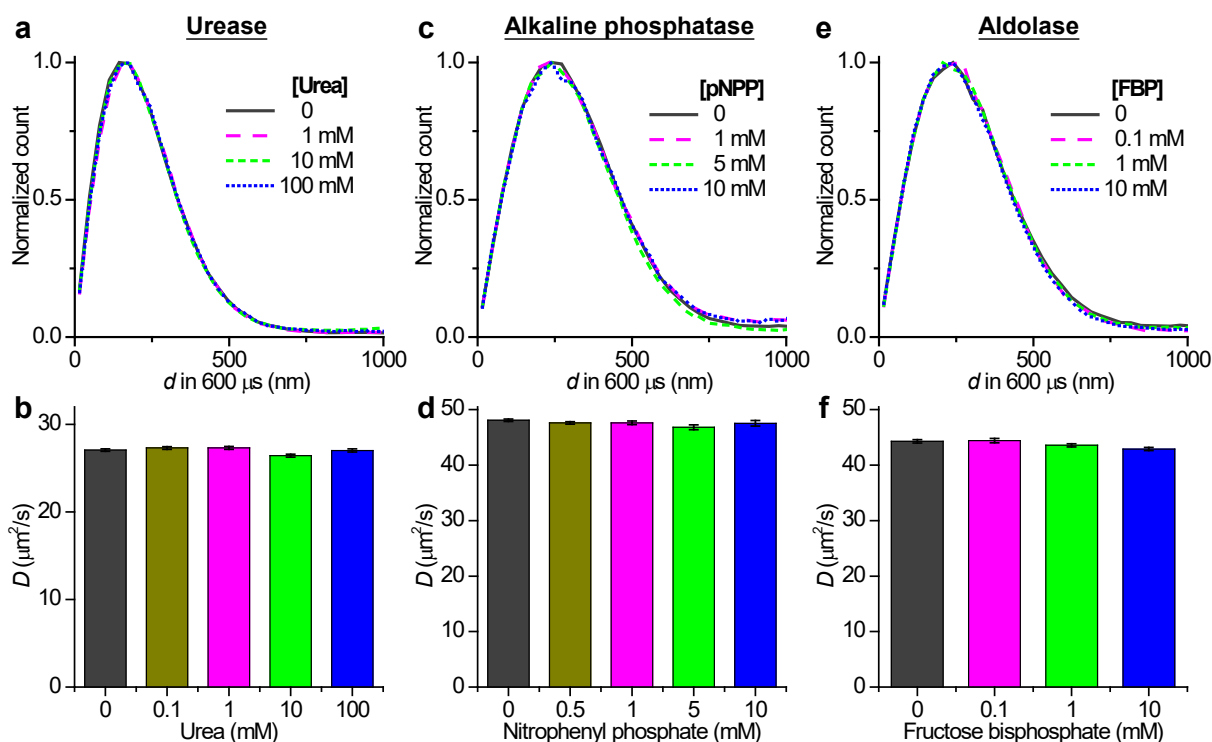
Figure 24. Results on urease, alkaline phosphatase, and aldolase also show no changes in single-molecule displacements under catalytic turnover.

(a) Normalized distributions of the measured 600-µs single-molecule displacements for Cy3B-labeled urease in PBS, with and without the addition of urea at different concentrations. (b) MLE-determined D values at different urea concentrations. Error bars: 95% confidence intervals of MLE. (c,d) Similar to that in (a,b), but for Cy3B-labeled alkaline phosphatase in 0.1 M Tris-HCl (pH = 9.8) with the addition of 1 mM $MgCl_2$ and 20 µM $ZnCl_2$, with p-nitrophenyl phosphate (pNPP) as the substrate. (e,f) Similar to that in (a,b), but for Cy3B-labeled aldolase in 0.1 M HEPES (pH = 7.4), with fructose 1,6-bisphosphate (FBP) as the substrate.

4.1.4. Conclusion

Together, with the high precision achieved through the high single-molecule statistics of SMdM, our results consistently showed unvarying D for four enzymes that have been reported as exhibiting enhanced diffusion under catalytic turnovers. These results, together with recent experiments that reexamine artifacts due to photophysical processes as fluorescence quenching and blinking,[107,121,122] underscore the difficulties with quantifying D through FCS. Although blinking-suppressing buffers partly alleviate these issues while also enabling single-molecule trapping for D measurements,[122] the addition of reducing and oxidizing chemicals complicates data interpretation. Meanwhile, the high D values of enzymes have largely limited single-molecule

tracking to systems in which viscous reagents as methylcellulose[132,133] and glycerol[122,133] are added to slow down molecular motions.

In contrast, with SM*d*M we were able to work with the diffusion of enzymes in regular buffers without the addition of extraneous components that may potentially affect the system: As SM*d*M captured and accumulated the transient (600 µs) displacements of single molecules, it removed the needs to establish long-term fluorophore photostability or to impede diffusion to permit multi-frame tracking. Whereas in this study we have employed MLE to extract D values based on normal (Gaussian) diffusion, the highly invariant distributions of single-molecule displacements we observed under different substrate concentrations suggest no changes in diffusivity independent of the specific model. The sub-millisecond motion-detection time window of SM*d*M is comparable to that of FCS, which has been the primary method used in previous studies to advocate enhanced diffusion in the presence of substrates. For the four enzymes examined, this time window should accommodate multiple turnovers for catalase, urease, and ALP, but not aldolase. Our results thus support recent analysis that reaction-facilitated diffusion vanishes at the molecular scale,[112] and call for the reexamination of factors that may have inadvertently affected previous measurements, including both photophysical processes[107,121,122] and the dissociation of enzyme subunits.[107,118] The application of the tools developed in this work to other systems in which precise D values are important, potentially including the even faster diffusion of smaller molecules, awaits future efforts.

4.2. Multi-component models for SM*d*M data analysis

All previous results of SM*d*M assumed a single-component model in MLE:

$$pdf(r) \propto \frac{2r}{4D\Delta t} \exp\left(-\frac{r^2}{4D\Delta t}\right) + br \tag{4.1}$$

where *pdf*(*r*) is the radial probability distribution function (pdf), r is step displacement in time interval Δt, D is diffusion coefficient. For simplicity, the normalization factor is not shown. b accounts for matching extraneous molecules rather than the identical molecule when calculating r. This term is proportional to the density of the target molecule. However, in practice, multiple species can be detected in a single color channel, *i.e.*, contamination or the target under equilibrium of multiple states. For example, SM*d*M of a protein under monomeric-dimeric equilibrium will result in the step displacement distribution that does not follow equation 4.1. To correctly fit the data, modification to the model is necessary:

$$pdf(r) \propto p \frac{2r}{4D_1\Delta t} \exp\left(-\frac{r^2}{4D_1\Delta t}\right) + (1-p) \frac{2r}{4D_2\Delta t} \exp\left(-\frac{r^2}{4D_2\Delta t}\right) + br \tag{4.2}$$

where D_1 and D_2 are diffusion coefficients of two components, respectively, and p is the fraction of the first component among the captured step displacements. Note that p and $(1-p)$ do not directly project an actual population ratio under equilibrium, as even with the same concentration, species diffusing faster has a lower chance to be traced in the paired frame. Likewise, n-component models can be introduced for MLE in SMdM, *i.e.*, the three-component model will be:

$$pdf(r) \propto p\frac{2r}{4D_1\Delta t}\exp\left(-\frac{r^2}{4D_1\Delta t}\right) + q\frac{2r}{4D_2\Delta t}\exp\left(-\frac{r^2}{4D_2\Delta t}\right) + (1-p-q)\frac{2r}{4D_3\Delta t}\exp\left(-\frac{r^2}{4D_3\Delta t}\right) + br \quad (4.3)$$

with D_1, D_2, and D_3 being the diffusion coefficients of the three components, and p and q being the fractions of the first and the second components, respectively. As increasing the number of parameters to fit the data steadily decreases the residual, the most suitable model for a given data should be determined from the likelihood-ratio test. With the collection of the step distance data, $\hat{X}$, the likelihood (L) of one model is calculated as a product of the probability of all data under the model pdf. For example, for the single-component model above, the likelihood is given as:

$$L_{single} = \prod pdf(\hat{X}), \; with \; pdf(r) \propto \frac{2r}{4D\Delta t}\exp\left(-\frac{r^2}{4D\Delta t}\right) + br \quad (4.4)$$

For the statistical test, the negative log of the likelihood ratio (λ_{LR}) of MLE results is calculated:

$$\lambda_{\text{LR}} = -2 \ln\left[\frac{L_{constrained}}{L_{unconstrained}}\right] \quad (4.5)$$

where the constrained model is the model assuming fewer components. With the cumulative distribution function (CDF) of chi-squared distribution with k degrees of freedom[134], χ_k^2, where k is the difference in the number of parameters between the two models: For example, $k = 2$ when comparing the single-component (D, b) and two-component (D_1, D_2, p, b), or two-component and three-component (D_1, D_2, D_3, p, q, b) models. The CDF value at $x = \lambda_{\text{LR}}$ thus equals $(1 - p\text{-value})$, and that low p-value indicates the statistical significance to keep the unconstrained model. Practically, a significance level of 0.05 or 0.001 can be set as a standard, then λ_{LR} is compared to the fixed value at given k (for example, if $k = 2$, these are 5.99 and 13.82, respectively). In this section, I will discuss verifying the multi-component models for SMdM analysis as a proof of the concept, first on simulated data and then on experimental data that successfully distinguish two different species.

4.2.1. Validation of multi-component models using simulated data

To compare single- and multi-component models in MLE of SMdM data, I generated collections of step displacements under the probability distribution of eqn. 4.2. As typical proteins in the physiological condition have diffusion coefficients of tens of $\mu m^2/s$, the simulation was performed for D_1 and D_2 both in the range of 1~60 $\mu m^2/s$. The population p was swept from 0 to 1, and Δt was fixed to 1 ms for simplicity and to replicate typical SMdM data acquisitions. Although the total count of step displacement was also a parameter to sweep at the initial stage,

counts over 10,000 showed no significant trend by the data size and were not differentiated here and below. For each combination of parameters, 100 independent simulations were performed for statistical robustness.
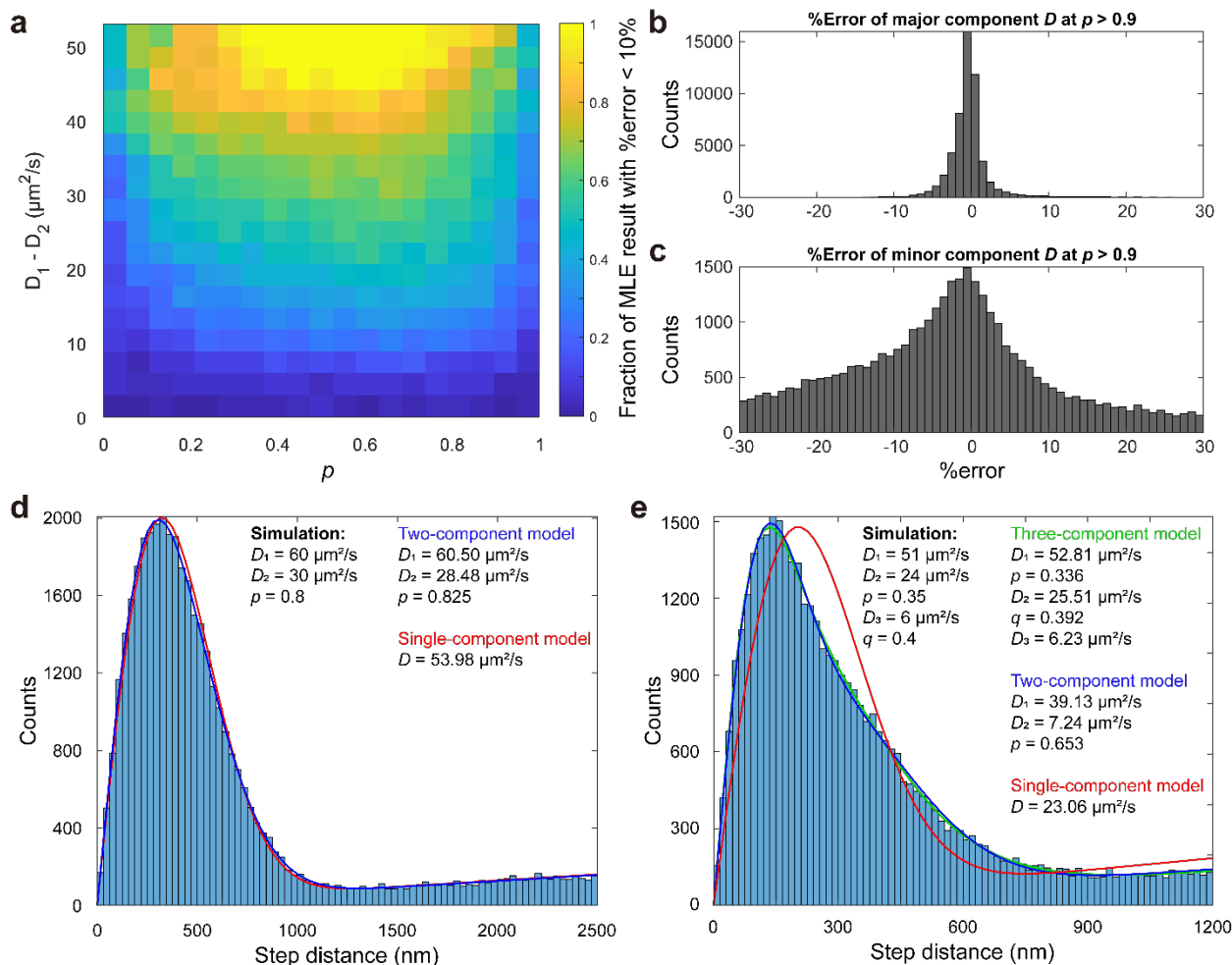
Figure 25. Multi-component MLE results on Simulated SM*d*M data.
(a) Probability diagram of two-component MLE result predicts all D_1, D_2, and p within 10% relative error to the ground truth. (b) %Error distribution of D_1 at $p > 0.9$ and D_2 at $p < 0.1$. (c) %Error distribution of D_1 at $p < 0.1$ and D_2 at $p > 0.9$. (d) Histogram: the count distribution of 40,000 step displacement generated with $D_1 = 60$ μm²/s, $D_2 = 30$ μm²/s, and $p = 0.8$ from eqn. 4.2. Red line: Single-component MLE result. Blue line: Two-component MLE result. (e) Histogram: the count distribution of 40,000 step displacement generated with $D_1 = 51$ μm²/s, $D_2 = 24$ μm²/s, $D_3 = 6$ μm²/s, $p = 0.35$ and $q = 0.4$ from eqn. 4.3. Red line: Single-component MLE result. Blue line: Two-component MLE result. Green line: Three-component MLE result.

     Extensive qualification of two-component MLE performance by ground truth conditions, diffusivity difference between two species and their population, is summarized in Figure 25a. As nearly all data of *p* range in 0.1~0.9 passed the likelihood-ratio test, the fraction of the MLE results having relative errors for D_1, D_2, and *p* all less than 10% are shown for validation of two-

component MLE. When one species outnumbers the other by a huge extent, the MLE result was not accurate regardless of the D difference. However, the D of the major component was accurately analyzed (Figure 25b), and the inaccuracy was explicitly from the diffusivity of the minor component (Figure 25c) and the population (for example, MLE result of $p = 0.06$ is outside 10% error from $p = 0.05$). In moderately populated circumstances, the MLE performed with high accuracy when the D difference was at least 20-30 μm^2/s. The results together set the guideline for two-component MLE in SMdM data, of which system the model would provide the correct picture.

For instance, 30,000 step distances generated with 70% of 35 μm^2/s and 30% of 12 μm^2/s, the single-component MLE yielded 26.66 μm^2/s (Figure 25d, red line), whereas two-component MLE correctly differentiated two diffusivities as 35.51 μm^2/s and 11.93 μm^2/s, with 68.8% and 31.2% population, respectively (Figure 25d, blue line). As SMdM analysis of similar data size gives <10% of error (Figure 22c), ~30% error from the diffusivity of the main component implies a two-component model is necessary for the data. Indeed, the log-likelihood test for comparing models strongly suggested the two-component over the single-component with p-value < 0.001.

To further validate the multi-component model with simulated data, a set of 40,000 step distances were generated from eqn. 4.3. with 35% of 51 μm^2/s, 40% of 24 μm^2/s, 25% of 6 μm^2/s (Figure 25e, histogram). From the heterogeneous data, the single-component MLE yielded 23.06 μm^2/s (Figure 25e, red line), the two-component MLE fitted two diffusivities as 39.13 μm^2/s and 7.24 μm^2/s, with 65.3% and 34.7% population, respectively (Figure 25e, blue line), and the three-component MLE correctly differentiated the three diffusivities as 52.81 μm^2/s, 25.51 μm^2/s, and 6.23 μm^2/s, with 33.6%, 39.2%, and 27.2% population, respectively (Figure 25e, green line). While both multi-component models performed better fitting over the single-component model and yielded comparable curves, the two-component MLE resulted in faster diffusivity of nearly an average value of two faster components and even failed to predict the correct fraction of the slowest component. This was further statistically verified from the negative log-likelihood ratio of the two models being ~18.9, which corresponds to a p-value < 0.001 and imply the three-component model is suitable for the given data.

4.2.2. Application for heterogeneous protein samples

To demonstrate the application of the two-component MLE in SMdM data analysis, here I present two cases where using the model was found effective: distinguishing two species in a single color channel and identifying two different states of proteins in the heterogeneous system. Firstly, the model clearly identified both Cy3B-labeled BSA and the free form of Cy3B in a single sample (Figure 26a). Not only the step distance histogram was successfully fitted with the two-component model (Figure 26a, blue line), the D of both BSA-Cy3B and Cy3B in PBS were correctly analyzed: here 59.36 μm^2/s and 370.05 μm^2/s, respectively, compared to 57±2 μm^2/s and 357±10 μm^2/s (95% confidence intervals of MLE), respectively when BSA and Cy3B are separately measured (Figure 5b). Consistent with the visual assessment, λ_{LR} of the two models was

over 1300. Meanwhile, λ_{LR} between the two- and three-component models was negative as the three-component MLE failed to converge, and the likelihood was not maximized. Thus, the two-component model was the most suitable for the data. Although the chemical labeling of proteins with the dyes are followed by thorough filtering and purification, some chemical and physical conditions such as pH may lead to the dissociation of the bond and generate impurities. As SMdM can track fast diffusing free dyes, it can qualify the purity of the protein sample with high sensitivity in 1-2 minutes of data collection.
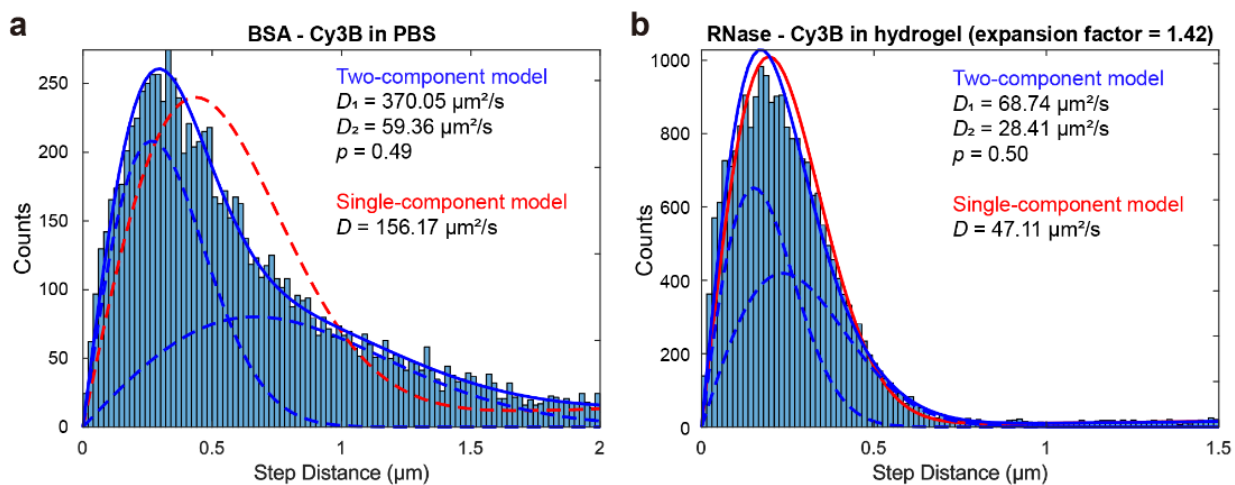

Figure 26. Single- and two-component MLE results on SM*d*M data.

(a) Histogram: the count distribution of SMdM step displacements of BSA-Cy3B containing free Cy3B dissociated under basic pH at 600 µs time interval. Red line: Single-component MLE result. Blue line: Two-component MLE result. The solid line shows the fitted scaled probability distribution, and dashed lines show fitted step distance distribution for the two species separately. (b) Histogram: the count distribution of SMdM step displacements in 400 µs time interval of RNase A-Cy3B in the hydrogel of expansion factor 1.42. See chapter 2 for detailed experimental conditions. The labeled protein here was not passivated to remove the excessive surface positive charges. Red line: Single-component MLE result. Blue line: Two-component MLE result. The solid line shows the fitted scaled probability distribution, and dashed lines show fitted step distance distribution for the two species separately.

The two-component MLE can also discriminate two states of a single protein. For the RNase A in the hydrogel presented in Chapter 2 where it exhibits decreased diffusivity compared to in PBS, two distinctive D was analyzed (Figure 26b). While RNase A in the hydrogel with an expansion factor of 1.42 (2.9× volume expansion; 3.1 wt % final polymer content) is expected to have diffusivity around 70 µm^2/s (Figure 6a), the single-component MLE resulted in 47.11 µm^2/s. Unlike results presented in Chapter 2, here the positive charges of RNase A were not passivated with the acetate functional group. As RNase A is a protein positively charged under physiological pH (pI = 9.6), the protein experiences extra hindrance from charge interactions in the hydrogel of negatively charged acrylate.[16] Such an effect was not observed from all of the proteins in the sample, as the fluorescence labeling degree varies protein by protein: one can have a single dye

conjugated, while another protein can have all available lysine residue consumed. The partially labeled protein would experience the charge effect, whereas fully labeled proteins are only affected by the geometric environment in the hydrogel. This was reflected in two different diffusivities from the SMdM data, that one population has 68.74 μm^2/s, which corresponds to RNase A only experiencing steric effect of the meshwork, and the other has even slower diffusion, 28.41 μm^2/s (Figure 26b, blue dashed lines). Here λ_{LR} of two models was over 320, and between the two- and three-component model was negative as three-component MLE also failed to converge. This again indicated the two-component model was the best, but not more component. Together, the multi-component model for MLE of the SMdM data revealed deeper insight those are not explicitly available from the single-component model. For more complex systems, this can be further extended to higher degree of multi-component model for SMdM MLE.

References

1. Atkins, P. W. & De Paula, J. *Physical chemistry*. (W.H. Freeman, 2010).

2. Moerner, W. E. & Fromm, D. P. Methods of single-molecule fluorescence spectroscopy and microscopy. *Rev. Sci. Instrum.* **74**, 3597–3619 (2003).

3. Joo, C., Balci, H., Ishitsuka, Y., Buranachai, C. & Ha, T. Advances in Single-Molecule Fluorescence Methods for Molecular Biology. *Annu. Rev. Biochem.* **77**, 51–76 (2008).

4. *Advanced optical methods for brain imaging*. (Springer Berlin Heidelberg, 2018).

5. Murphy, D. B. & Davidson, M. W. *Fundamentals of light microscopy and electronic imaging*. (Wiley-Blackwell, 2013).

6. Rust, M. J., Bates, M. & Zhuang, X. Sub-diffraction-limit imaging by stochastic optical reconstruction microscopy (STORM). *Nat. Methods* **3**, 793–796 (2006).

7. Betzig, E. *et al.* Imaging Intracellular Fluorescent Proteins at Nanometer Resolution. *Science* **313**, 1642–1645 (2006).

8. Sharonov, A. & Hochstrasser, R. M. Wide-field subdiffraction imaging by accumulated binding of diffusing probes. *Proc. Natl. Acad. Sci.* **103**, 18911–18916 (2006).

9. Thompson, R. E., Larson, D. R. & Webb, W. W. Precise Nanometer Localization Analysis for Individual Fluorescent Probes. *Biophys. J.* **82**, 2775–2783 (2002).

10. Xu, K., Zhong, G. & Zhuang, X. Actin, Spectrin, and Associated Proteins Form a Periodic Cytoskeletal Structure in Axons. *Science* **339**, 452–456 (2013).

11. Ricci, M. A., Manzo, C., García-Parajo, M. F., Lakadamyali, M. & Cosma, M. P. Chromatin Fibers Are Formed by Heterogeneous Groups of Nucleosomes In Vivo. *Cell* **160**, 1145–1158 (2015).

12. Bintu, B. *et al.* Super-resolution chromatin tracing reveals domains and cooperative interactions in single cells. *Science* **362**, eaau1783 (2018).

13. Sigal, Y. M., Zhou, R. & Zhuang, X. Visualizing and discovering cellular structures with super-resolution microscopy. *Science* **361**, 880–887 (2018).

14. Xiang, L., Chen, K. & Xu, K. Single Molecules Are Your Quanta: A Bottom-Up Approach toward Multidimensional Super-resolution Microscopy. *ACS Nano* **15**, 12483–12496 (2021).

15. Moon, S. *et al.* Spectrally Resolved, Functional Super-Resolution Microscopy Reveals Nanoscale Compositional Heterogeneity in Live-Cell Membranes. *J. Am. Chem. Soc.* **139**, 10944–10947 (2017).

16. Xiang, L., Chen, K., Yan, R., Li, W. & Xu, K. Single-molecule displacement mapping unveils nanoscale heterogeneities in intracellular diffusivity. *Nat. Methods* **17**, 524–530 (2020).

17. Chen, F., Tillberg, P. W. & Boyden, E. S. Expansion microscopy. *Science* **347**, 543–548 (2015).

18. Wassie, A. T., Zhao, Y. & Boyden, E. S. Expansion microscopy: principles and uses in biological research. *Nat. Methods* **16**, 33 (2019).

19. Park, H. H., Choi, A. A. & Xu, K. Size-Dependent Suppression of Molecular Diffusivity in Expandable Hydrogels: A Single-Molecule Study. *J. Phys. Chem. B* **127**, 3333–3339 (2023).

20. Verkman, A. S. Solute and macromolecule diffusion in cellular aqueous compartments. *Trends Biochem. Sci.* **27**, 27–33 (2002).

21. Soh, S., Byrska, M., Kandere-Grzybowska, K. & Grzybowski, B. A. Reaction-Diffusion Systems in Intracellular Molecular Transport and Control. *Angew. Chem. Int. Ed.* **49**, 4170–4198 (2010).

22. Shen, H. *et al.* Single Particle Tracking: From Theory to Biophysical Applications. *Chem. Rev.* **117**, 7331–7376 (2017).

23. Mogre, S. S., Brown, A. I. & Koslover, E. F. Getting around the cell: physical transport in the intracellular world. *Phys. Biol.* **17**, 061003 (2020).

24. Milo, R. & Phillips, R. *Cell Biology by the Numbers*. (Garland Science, 2015). doi:10.1201/9780429258770.

25. Lukacs, G. L. *et al.* Size-dependent DNA Mobility in Cytoplasm and Nucleus *. *J. Biol. Chem.* **275**, 1625–1629 (2000).

26. Dauty, E. & Verkman, A. S. Actin Cytoskeleton as the Principal Determinant of Size-dependent DNA Mobility in Cytoplasm: A NEW BARRIER FOR NON-VIRAL GENE DELIVERY*. *J. Biol. Chem.* **280**, 7823–7828 (2005).

27. Kumar, M., Mommer, M. S. & Sourjik, V. Mobility of Cytoplasmic, Membrane, and DNA-Binding Proteins in Escherichia coli. *Biophys. J.* **98**, 552–559 (2010).

28. Kalwarczyk, T. *et al.* Comparative Analysis of Viscosity of Complex Liquids and Cytoplasm of Mammalian Cells at the Nanoscale. *Nano Lett.* **11**, 2157–2163 (2011).

29. Śmigiel, W. M. *et al.* Protein diffusion in Escherichia coli cytoplasm scales with the mass of the complexes and is location dependent. *Sci. Adv.* **8**, eabo5387 (2022).

30. Choi, A. A., Xiang, L., Li, W. & Xu, K. Single-Molecule Displacement Mapping Indicates Unhindered Intracellular Diffusion of Small ($\leqslant$1 kDa) Solutes. *J. Am. Chem. Soc.* **145**, 8510–8516 (2023).

31. Fushimi, K. & Verkman, A. S. Low viscosity in the aqueous domain of cell cytoplasm measured by picosecond polarization microfluorimetry. *J. Cell Biol.* **112**, 719–725 (1991).

32. Li, J. & Mooney, D. J. Designing hydrogels for controlled drug delivery. *Nat. Rev. Mater.* **1**, (2016).

33. Saini, A. & Kisley, L. Fluorescence microscopy of biophysical protein dynamics in nanoporous hydrogels. *J. Appl. Phys.* **126**, 081101 (2019).

34. Guo, Y. *et al.* Hydrogels and Hydrogel-Derived Materials for Energy and Water Sustainability. *Chem. Rev.* **120**, 7642–7707 (2020).

35. Yuk, H., Wu, J. & Zhao, X. Hydrogel interfaces for merging humans and machines. *Nat. Rev. Mater.* **7**, 935–952 (2022).

36. Kisley, L. *et al.* Characterization of Porous Materials by Fluorescence Correlation Spectroscopy Super-resolution Optical Fluctuation Imaging. *ACS Nano* **9**, 9158–9166 (2015).

37. Sandrin, D. *et al.* Diffusion of macromolecules in a polymer hydrogel: from microscopic to macroscopic scales. *Phys. Chem. Chem. Phys.* **18**, 12860–12876 (2016).

38. Offeddu, G. S., Axpe, E., Harley, B. A. C. & Oyen, M. L. Relationship between permeability and diffusivity in polyethylene glycol hydrogels. *AIP Adv.* **8**, 105006 (2018).

39. Kremer, M. *et al.* Pore-Size Distributions of Cationic Polyacrylamide Hydrogels Varying in Initial Monomer Concentration and Cross-Linker/Monomer Ratio. *Macromolecules* **27**, 2965–2973 (1994).

40. Zwettler, F. U. *et al.* Molecular resolution imaging by post-labeling expansion single-molecule localization microscopy (Ex-SMLM). *Nat. Commun.* **11**, 3388 (2020).

41. Kang, M., Lee, J., Ko, S. & Shim, S.-H. Prelabeling Expansion Single-Molecule Localization Microscopy with Minimal Linkage Error. *ChemBioChem* **22**, 1396–1399 (2021).

42. Lee, H., Yu, C.-C., Boyden, E. S., Zhuang, X. & Kosuri, P. Tetra-gel enables superior accuracy in combined super-resolution imaging and expansion microscopy. *Sci. Rep.* **11**, 16944 (2021).

43. Shi, X. *et al.* Label-retention expansion microscopy. *J. Cell Biol.* **220**, e202105067 (2021).

44. Yan, R., Chen, K. & Xu, K. Probing Nanoscale Diffusional Heterogeneities in Cellular Membranes through Multidimensional Single-Molecule and Super-Resolution Microscopy. *J. Am. Chem. Soc.* **142**, 18866–18873 (2020).

45. Choi, A. A. *et al.* Displacement Statistics of Unhindered Single Molecules Show no Enhanced Diffusion in Enzymatic Reactions. *J. Am. Chem. Soc.* **144**, 4839–4844 (2022).

46. Xie, X. S., Yu, J. & Yang, W. Y. Living Cells as Test Tubes. *Science* **312**, 228–230 (2006).

47. Xie, X. S., Choi, P. J., Li, G.-W., Lee, N. K. & Lia, G. Single-Molecule Approach to Molecular Biology in Living Bacterial Cells. *Annu. Rev. Biophys.* **37**, 417–444 (2008).

48. Tanaka, T. *et al.* Phase Transitions in Ionic Gels. *Phys. Rev. Lett.* **45**, 1636–1639 (1980).

49. Ohmine, I. & Tanaka, T. Salt effects on the phase transition of ionic gels. *J. Chem. Phys.* **77**, 5725–5729 (1982).

50. Young, M. E., Carroad, P. A. & Bell, R. L. Estimation of diffusion coefficients of proteins. *Biotechnol. Bioeng.* **22**, 947–955 (1980).

51. Cohen, Y., Ramon, O., Kopelman, I. J. & Mizrahi, S. Characterization of inhomogeneous polyacrylamide hydrogels. *J. Polym. Sci. Part B Polym. Phys.* **30**, 1055–1067 (1992).

52. sheely, M. L. Glycerol Viscosity Tables. *Ind. Eng. Chem.* **24**, 1060–1064 (1932).

53. Wang, Q. & Moerner, W. E. Single-molecule motions enable direct visualization of biomolecular interactions in solution. *Nat. Methods* **11**, 555–558 (2014).

54. Axpe, E. *et al.* A Multiscale Model for Solute Diffusion in Hydrogels. *Macromolecules* **52**, 6889–6897 (2019).

55. Asano, S. M. *et al.* Expansion Microscopy: Protocols for Imaging Proteins and RNA in Cells and Tissues. *Curr. Protoc. Cell Biol.* **80**, e56 (2018).

56. Truckenbrodt, S., Sommer, C., Rizzoli, S. O. & Danzl, J. G. A practical guide to optimization in X10 expansion microscopy. *Nat. Protoc.* **14**, 832 (2019).

57. Park, H. H., Wang, B., Moon, S., Jepson, T. & Xu, K. Machine-learning-powered extraction of molecular diffusivity from single-molecule images for super-resolution mapping. *Commun. Biol.* **6**, 1–8 (2023).

58. Lippincott-Schwartz, J., Snapp, E. & Kenworthy, A. Studying protein dynamics in living cells. *Nat. Rev. Mol. Cell Biol.* **2**, 444–456 (2001).

59. Macháň, R. & Wohland, T. Recent applications of fluorescence correlation spectroscopy in live systems. *FEBS Lett.* **588**, 3571–3584 (2014).

60. Lippincott-Schwartz, J., Snapp, E. L. & Phair, R. D. The Development and Enhancement of FRAP as a Key Tool for Investigating Protein Dynamics. *Biophys. J.* **115**, 1146–1155 (2018).

61. Wawrezinieck, L., Rigneault, H., Marguet, D. & Lenne, P.-F. Fluorescence Correlation Spectroscopy Diffusion Laws to Probe the Submicron Cell Membrane Organization. *Biophys. J.* **89**, 4029–4042 (2005).

62. Bacia, K., Kim, S. A. & Schwille, P. Fluorescence cross-correlation spectroscopy in living cells. *Nat. Methods* **3**, 83–89 (2006).

63. Elson, E. L. Fluorescence Correlation Spectroscopy: Past, Present, Future. *Biophys. J.* **101**, 2855–2870 (2011).

64. Krieger, J. W. *et al.* Imaging fluorescence (cross-) correlation spectroscopy in live cells and organisms. *Nat. Protoc.* **10**, 1948–1974 (2015).

65. Manley, S. *et al.* High-density mapping of single-molecule trajectories with photoactivated localization microscopy. *Nat. Methods* **5**, 155–157 (2008).

66. Chenouard, N. *et al.* Objective comparison of particle tracking methods. *Nat. Methods* **11**, 281–289 (2014).

67. Cognet, L., Leduc, C. & Lounis, B. Advances in live-cell single-particle tracking and dynamic super-resolution imaging. *Curr. Opin. Chem. Biol.* **20**, 78–85 (2014).

68. Manzo, C. & Garcia-Parajo, M. F. A review of progress in single particle tracking: from methods to biophysical insights. *Rep. Prog. Phys.* **78**, 124601 (2015).

69. Beheiry, M. E., Dahan, M. & Masson, J.-B. InferenceMAP: mapping of single-molecule dynamics with Bayesian inference. *Nat. Methods* **12**, 594–595 (2015).

70. Schuster, J., Cichos, F. & von Borczyskowski, C. Diffusion Measurements by Single-Molecule Spot-Size Analysis. *J. Phys. Chem. A* **106**, 5403–5406 (2002).

71. Zareh, S. K., DeSantis, M. C., Kessler, J. M., Li, J.-L. & Wang, Y. M. Single-Image Diffusion Coefficient Measurements of Proteins in Free Solution. *Biophys. J.* **102**, 1685–1691 (2012).

72. Serag, M. F., Abadi, M. & Habuchi, S. Single-molecule diffusion and conformational dynamics by spatial integration of temporal fluctuations. *Nat. Commun.* **5**, 5123 (2014).

73. Möckl, L., Roy, A. R. & Moerner, W. E. Deep learning in single-molecule microscopy: fundamentals, caveats, and recent developments [Invited]. *Biomed. Opt. Express* **11**, 1633–1661 (2020).

74. Nehme, E., Weiss, L. E., Michaeli, T. & Shechtman, Y. Deep-STORM: super-resolution single-molecule microscopy by deep learning. *Optica* **5**, 458–464 (2018).

75. Zhang, P. *et al.* Analyzing complex single-molecule emission patterns with deep learning. *Nat. Methods* **15**, 913–916 (2018).

76. Zelger, P. *et al.* Three-dimensional localization microscopy using deep learning. *Opt. Express* **26**, 33166–33179 (2018).

77. Kim, T., Moon, S. & Xu, K. Information-rich localization microscopy through machine learning. *Nat. Commun.* **10**, 1996 (2019).

78. Hershko, E., Weiss, L. E., Michaeli, T. & Shechtman, Y. Multicolor localization microscopy and point-spread-function engineering by deep learning. *Opt. Express* **27**, 6158–6183 (2019).

79. Möckl, L., Petrov, P. N. & Moerner, W. E. Accurate phase retrieval of complex 3D point spread functions with deep residual neural networks. *Appl. Phys. Lett.* **115**, 251106 (2019).

80. Zhang, Z., Zhang, Y., Ying, L., Sun, C. & Zhang, H. F. Machine-learning based spectral classification for spectroscopic single-molecule localization microscopy. *Opt. Lett.* **44**, 5864–5867 (2019).

81. Gaire, S. K. *et al.* Accelerating multicolor spectroscopic single-molecule localization microscopy using deep learning. *Biomed. Opt. Express* **11**, 2705–2721 (2020).

82. Möckl, L., Roy, A. R., Petrov, P. N. & Moerner, W. E. Accurate and rapid background estimation in single-molecule localization microscopy using the deep neural network BGnet. *Proc. Natl. Acad. Sci.* **117**, 60–67 (2020).

83. Nehme, E. *et al.* DeepSTORM3D: dense 3D localization microscopy and PSF design by deep learning. *Nat. Methods* **17**, 734–740 (2020).

84. Speiser, A. *et al.* Deep learning enables fast and dense single-molecule localization with high accuracy. *Nat. Methods* **18**, 1082–1090 (2021).

85. Cascarano, P. *et al.* DeepCEL0 for 2D single-molecule localization in fluorescence microscopy. *Bioinformatics* **38**, 1411–1419 (2022).

86. Spilger, R. *et al.* Deep Particle Tracker: Automatic Tracking of Particles in Fluorescence Microscopy Images Using Deep Learning. in *Deep Learning in Medical Image Analysis and Multimodal Learning for Clinical Decision Support* (eds. Stoyanov, D. et al.) vol. 11045 128–136 (Springer International Publishing, 2018).

87. Newby, J. M., Schaefer, A. M., Lee, P. T., Forest, M. G. & Lai, S. K. Convolutional neural networks automate detection for tracking of submicron-scale particles in 2D and 3D. *Proc. Natl. Acad. Sci.* **115**, 9026–9031 (2018).

88. Muñoz-Gil, G. *et al.* Objective comparison of methods to decode anomalous diffusion. *Nat. Commun.* **12**, 6253 (2021).

89. Kowalek, P., Loch-Olszewska, H. & Szwabiński, J. Classification of diffusion modes in single-particle tracking data: Feature-based versus deep-learning approach. *Phys. Rev. E* **100**, 032410 (2019).

90. Granik, N. *et al.* Single-Particle Diffusion Characterization by Deep Learning. *Biophys. J.* **117**, 185–192 (2019).

91. Pinholt, H. D., Bohr, S. S.-R., Iversen, J. F., Boomsma, W. & Hatzakis, N. S. Single-particle diffusional fingerprinting: A machine-learning framework for quantitative analysis of heterogeneous diffusion. *Proc. Natl. Acad. Sci.* **118**, e2104624118 (2021).

92. Pineda, J. *et al.* Geometric deep learning reveals the spatiotemporal features of microscopic motion. *Nat. Mach. Intell.* **5**, 71–82 (2023).

93. He, K., Zhang, X., Ren, S. & Sun, J. Deep Residual Learning for Image Recognition. in *2016 IEEE Conference on Computer Vision and Pattern Recognition (CVPR)* 770–778 (IEEE, 2016). doi:10.1109/CVPR.2016.90.

94. Ioffe, S. & Szegedy, C. Batch Normalization: Accelerating Deep Network Training by Reducing Internal Covariate Shift. in *Proceedings of the 32nd International Conference on Machine Learning* 448–456 (PMLR, 2015).

95. Ramachandran, P., Zoph, B. & Le, Q. V. Searching for Activation Functions. *ArXiv171005941 Cs* (2017).

96. Nair, V. & Hinton, G. E. Rectified linear units improve restricted boltzmann machines. in *Proceedings of the 27th International Conference on International Conference on Machine Learning* 807–814 (Omnipress, 2010).

97. Tobin, J. *et al.* Domain Randomization for Transferring Deep Neural Networks from Simulation to the Real World. *ArXiv170306907 Cs* (2017).

98. Filippov, A., Orädd, G. & Lindblom, G. Sphingomyelin Structure Influences the Lateral Diffusion and Raft Formation in Lipid Bilayers. *Biophys. J.* **90**, 2086–2092 (2006).

99. Macháň, R. & Hof, M. Lipid diffusion in planar membranes investigated by fluorescence correlation spectroscopy. *Biochim. Biophys. Acta BBA - Biomembr.* **1798**, 1377–1391 (2010).

100. Tinevez, J.-Y. *et al.* TrackMate: An open and extensible platform for single-particle tracking. *Methods* **115**, 80–90 (2017).

101. Tarantino, N. *et al.* TNF and IL-1 exhibit distinct ubiquitin requirements for inducing NEMO–IKK supramolecular structures. *J. Cell Biol.* **204**, 231–245 (2014).

102. Maekawa, T. *et al.* Molecular diffusion and nano-mechanical properties of multi-phase supported lipid bilayers. *Phys. Chem. Chem. Phys.* **21**, 16686–16693 (2019).

103. Kuo, C. & Hochstrasser, R. M. Super-resolution Microscopy of Lipid Bilayer Phases. *J. Am. Chem. Soc.* **133**, 4664–4667 (2011).

104. Yan, R., Wang, B. & Xu, K. Functional super-resolution microscopy of the cell. *Curr. Opin. Chem. Biol.* **51**, 92–97 (2019).

105. Muddana, H. S., Sengupta, S., Mallouk, T. E., Sen, A. & Butler, P. J. Substrate Catalysis Enhances Single-Enzyme Diffusion. *J. Am. Chem. Soc.* **132**, 2110–2111 (2010).

106. Riedel, C. *et al.* The heat released during catalytic turnover enhances the diffusion of an enzyme. *Nature* **517**, 227–230 (2015).

107. Günther, J.-P., Börsch, M. & Fischer, P. Diffusion Measurements of Swimming Enzymes with Fluorescence Correlation Spectroscopy. *Acc. Chem. Res.* **51**, 1911–1920 (2018).

108. Agudo-Canalejo, J., Adeleke-Larodo, T., Illien, P. & Golestanian, R. Enhanced Diffusion and Chemotaxis at the Nanoscale. *Acc. Chem. Res.* **51**, 2365–2372 (2018).

109. Zhao, X., Gentile, K., Mohajerani, F. & Sen, A. Powering Motion with Enzymes. *Acc. Chem. Res.* **51**, 2373–2381 (2018).

110. Zhang, Y. & Hess, H. Enhanced Diffusion of Catalytically Active Enzymes. *ACS Cent. Sci.* **5**, 939–948 (2019).

111. Feng, M. & Gilson, M. K. Enhanced Diffusion and Chemotaxis of Enzymes. *Annu. Rev. Biophys.* **49**, 87–105 (2020).

112. Zhang, Y. & Hess, H. Chemically-powered swimming and diffusion in the microscopic world. *Nat. Rev. Chem.* **5**, 500–510 (2021).

113. Sengupta, S. *et al.* Enzyme Molecules as Nanomotors. *J. Am. Chem. Soc.* **135**, 1406–1414 (2013).

114. Illien, P. *et al.* Exothermicity Is Not a Necessary Condition for Enhanced Diffusion of Enzymes. *Nano Lett.* **17**, 4415–4420 (2017).

115. Jiang, L., Santiago, I. & Foord, J. Observation of nanoimpact events of catalase on diamond ultramicroelectrodes by direct electron transfer. *Chem. Commun.* **53**, 8332–8335 (2017).

116. Jee, A.-Y., Dutta, S., Cho, Y.-K., Tlusty, T. & Granick, S. Enzyme leaps fuel antichemotaxis. *Proc. Natl. Acad. Sci.* **115**, 14–18 (2018).

117. Jee, A.-Y., Cho, Y.-K., Granick, S. & Tlusty, T. Catalytic enzymes are active matter. *Proc. Natl. Acad. Sci.* **115**, (2018).

118. Jee, A.-Y., Chen, K., Tlusty, T., Zhao, J. & Granick, S. Enhanced Diffusion and Oligomeric Enzyme Dissociation. *J. Am. Chem. Soc.* **141**, 20062–20068 (2019).

119. Ghosh, S. *et al.* Motility of Enzyme-Powered Vesicles. *Nano Lett.* **19**, 6019–6026 (2019).

120. Jee, A.-Y., Tlusty, T. & Granick, S. Master curve of boosted diffusion for 10 catalytic enzymes. *Proc. Natl. Acad. Sci.* **117**, 29435–29441 (2020).

121. Kandula, H. N., Jee, A.-Y. & Granick, S. Robustness of FCS (Fluorescence Correlation Spectroscopy) with Quenchers Present. *J. Phys. Chem. A* **123**, 10184–10189 (2019).

122. Chen, Z. *et al.* Single-molecule diffusometry reveals no catalysis-induced diffusion enhancement of alkaline phosphatase as proposed by FCS experiments. *Proc. Natl. Acad. Sci.* **117**, 21328–21335 (2020).

123. Zhang, Y., Armstrong, M. J., Bassir Kazeruni, N. M. & Hess, H. Aldolase Does Not Show Enhanced Diffusion in Dynamic Light Scattering Experiments. *Nano Lett.* **18**, 8025–8029 (2018).

124. Pavlick, R. A., Dey, K. K., Sirjoosingh, A., Benesi, A. & Sen, A. A catalytically driven organometallic molecular motor. *Nanoscale* **5**, 1301–1304 (2013).

125. Günther, J.-P., Majer, G. & Fischer, P. Absolute diffusion measurements of active enzyme solutions by NMR. *J. Chem. Phys.* **150**, 124201 (2019).

126. MacDonald, T. S. C., Price, W. S., Astumian, R. D. & Beves, J. E. Enhanced Diffusion of Molecular Catalysts is Due to Convection. *Angew. Chem.* **131**, 19040–19043 (2019).

127. Wang, H. *et al.* Boosted molecular mobility during common chemical reactions. *Science* **369**, 537–541 (2020).

128. Günther, J.-P. *et al.* Comment on "Boosted molecular mobility during common chemical reactions". *Science* **371**, eabe8322 (2021).

129. Wang, H. *et al.* Response to Comment on "Boosted molecular mobility during common chemical reactions". *Science* **371**, eabe8678 (2021).

130. Ha, T. Single-molecule methods leap ahead. *Nat. Methods* **11**, 1015–1018 (2014).

131. Moerner, W. E., Shechtman, Y. & Wang, Q. Single-molecule spectroscopy and imaging over the decades. *Faraday Discuss.* **184**, 9–36 (2015).

132. Xu, M., Ross, J. L., Valdez, L. & Sen, A. Direct Single Molecule Imaging of Enhanced Enzyme Diffusion. *Phys. Rev. Lett.* **123**, 128101 (2019).

133. Xu, M., Rogers, W. B., Ahmed, W. W. & Ross, J. L. Comparison of different approaches to single-molecule imaging of enhanced enzyme diffusion. Preprint at https://doi.org/10.48550/arXiv.2012.15424 (2020).

134. Mood, A. M., Graybill, F. A. & Boes, D. C. *Introduction to the Theory of Statistics*. (McGraw-Hill, 1973).